

# Inversion techniques for optical conductivity data

E. Schachinger,<sup>1,\*</sup> D. Neuber,<sup>1</sup> and J.P. Carbotte<sup>2</sup>

<sup>1</sup>*Institute of Theoretical and Computational Physics*

*Graz University of Technology, A-8010 Graz, Austria*

<sup>2</sup>*Department of Physics and Astronomy, McMaster University,  
Hamilton, Ontario, L8S 4M1 Canada*

(Dated: December 20, 2018)

Optical data is encoded with information on the microscopic interaction between charge carriers. For an electron-phonon system, the Eliashberg equations apply and a Kubo formula can be used to get the infrared conductivity. The task of extracting the electron-phonon spectral density  $\alpha^2 F(\omega)$  from data is rather complicated and, thus, simplified but approximate expressions for the conductivity have often been used. We test the accuracy of such simplifications and also discuss the advantages and disadvantages of various numerical methods needed in the inversion process. Normal and superconducting state are considered as well as boson exchange mechanisms which might be applicable to the High- $T_c$  oxides.

PACS numbers: 74.20.Mn 74.25.Gz 74.72.-h

## I. INTRODUCTION

The interaction Hamiltonian between electrons and phonons involves a complicated matrix element or coupling function  $g_{\mathbf{k},\mathbf{k}',\nu}$  which describes the scattering of an electron initially in the state  $|\mathbf{k}\rangle$  to any final state  $|\mathbf{k}'\rangle$  through the exchange of a phonon  $\omega_\nu(\mathbf{k}' - \mathbf{k})$ . Here  $\nu$  is a phonon branch index and the momentum transfer  $\mathbf{k}' - \mathbf{k}$  can fall outside the first Brillouin zone and so phonon Umklapp processes enter. In a real metal the Bloch states of the band structure can be complicated and this is reflected in the electronic state labeled by  $|\mathbf{k}\rangle$ . Fortunately, many important properties of an electron-phonon system require for their understanding only a Fermi surface to Fermi surface average of the coupling, namely the function<sup>1</sup>

$$\alpha^2 F(\omega) = \frac{1}{N(\mu)} \sum_{\mathbf{k},\mathbf{k}'} B_\nu(\mathbf{k}' - \mathbf{k}) \delta(\varepsilon_{\mathbf{k}} - \mu) \delta(\varepsilon_{\mathbf{k}'} - \mu),$$

where  $\mu$  is the chemical potential,  $\varepsilon_{\mathbf{k}}$  the electron energy,  $N(\mu)$  the electron density of states and  $B_\nu(\mathbf{k}' - \mathbf{k})$  the phonon spectral function. For example, in the Eliashberg formulation<sup>2</sup> of superconductivity based on Migdal's theorem for electron-phonon vertex corrections, it is  $\alpha^2 F(\omega)$  that enters. For the infrared conductivity another, somewhat different weighting of  $g_{\mathbf{k},\mathbf{k}',\nu}$  comes in and the resulting function of  $\omega$  is usually called the transport spectral density denoted  $\alpha_{tr}^2 F(\omega)$ .<sup>3,4</sup> Here we will not deal directly with these differences. An important goal of experiments in conventional superconductors has been to determine the electron-phonon spectral function  $\alpha^2 F(\omega)$ .<sup>2,3</sup> This has been successfully accomplished for a large number of conventional materials using tunneling data and the inversion technique of McMillan and Rowell.<sup>5</sup> In a few cases the infrared optical conductivity<sup>6,7</sup> was also used and excellent agreement with tunneling results was found.

Extensions to the consideration of the A15 compounds revealed that additional features of the band structure

such as the energy dependence of the electronic density of states  $N(\varepsilon)$  can also be important.<sup>8,9</sup> More recently the optical data in the alkali doped  $C_{60}$  compounds has been inverted<sup>10</sup> and found consistent with its superconductivity. When experimentally determined electron-phonon spectral functions are compared with first principle band structure calculations extended to include electron-phonon interaction good agreement is obtained.<sup>2,7</sup>

In dealing with the high- $T_c$  oxides several complications immediately arise. First, their superconductivity is not generally believed to be due to the electron-phonon interaction. A consensus exists that the gap has  $d$ -wave rather than  $s$ -wave symmetry and comes out as a result of strong correlation effects. A natural explanation for the  $d$ -wave gap is found in the antiferromagnetic interaction certainly present in the cuprates. A possible model is the Nearly Antiferromagnetic Fermi Liquid model (NAFFL) of Pines and coworkers.<sup>11,12</sup> It needs to be pointed out, however, that there is no a priori reason why the electron-phonon interaction itself could not lead to a  $d$ -wave gap and there exists recent work on this possibility.<sup>13,14,15,16,17,18,19</sup> In any case, when  $d$ -wave symmetry is involved, the spectral function acting in the gap channel Eq. (B1a) need not be the same that determines the renormalizations in the  $\omega$ -channel Eq. (B1b). At  $T_c$  in the normal state it is only the latter spectral density that enters. There exists considerable literature on extensions of Eliashberg theory to include a  $d$ -wave gap based on model spectral densities for the electron-boson interaction that may be involved.<sup>20</sup> Of course, there is no guarantee that the final theory of strongly correlated systems that is needed to describe the oxides will fall within the class of boson exchange models. Nevertheless, such an approach has proven valuable in providing insight into the physics of the oxides as we will see also in this paper.

In the recent literature, tunneling spectroscopy<sup>21,22,23</sup> as well as angular resolved photo emission<sup>24,25,26,27,28</sup> has been used to analyze data in terms of boson structure.

Here we wish to concentrate on optical data.<sup>29,30,31,32</sup> Optimally doped YBa<sub>2</sub>Cu<sub>3</sub>O<sub>6.95</sub> (YBCO) was first considered within a complete Eliashberg formalism generalized to include *d*-wave pairing by Carbotte *et al.*<sup>29</sup> (CSB). A model form for the electron-boson spectral function coming possibly from exchange of spin fluctuations and denoted by  $I^2\chi(\omega)$  is assumed with two fitting parameters, the coupling  $I^2$  and the spin fluctuation energy  $\omega_{sf}$  in the model of Millis *et al.*<sup>33</sup> (MMP) which are fit to get the best fit to the normal state infrared data at  $T = T_c$ . For the superconducting state the same form of  $I^2\chi(\omega)$  is assumed to also determine the gap channel but its magnitude is different and is fit to get the measured value of  $T_c$ . In addition, it is found that the data in the superconducting state indicates the formation of an optical resonance in  $I^2\chi(\omega)$  not present at  $T_c$  which increases in amplitude as  $T$  is reduced and is positioned at 41 meV. Similar optical resonances were later found in the superconducting state of other cuprates although not in all.<sup>34</sup> In some the resonance seems to persist even in the normal state.<sup>31,35</sup> While the work described above involves a least squares fit of an assumed form for  $I^2\chi(\omega)$  to the optical scattering rate data other inversion techniques<sup>36</sup> have been considered but so far these are based on approximate analytic formulas for the relationship between the optical scattering rate and the electron-boson spectral density rather than the full Eliashberg formulation of Carbotte and coworkers.<sup>1,20,29,30</sup>

Such approximate formulas were given by Allen<sup>3</sup> for an electron-phonon system and are based on ordinary second order perturbation theory at zero temperature. Allen considered the normal as well as the superconducting state with *s*-wave symmetry. A generalization to finite temperature was provided by Shulga *et al.*<sup>37</sup> who only considered the normal state but started directly from an Eliashberg formalism and the Kubo formula for the conductivity. A generalization to include as well a pseudogap was recently provided by Sharapov and Carbotte.<sup>38</sup> Finally, Carbotte and Schachinger<sup>39</sup> generalized the original work of Allen to a superconductor with *d*-wave gap symmetry.

The advantage of these simplified but approximate equations is that they relate directly through an integral the optical scattering rate to the desired spectral function  $I^2\chi(\omega)$  and various numerical techniques such as singular value decomposition<sup>36,39</sup> can be used to numerically invert the equation. Of course, the alternate method of assuming some characteristic functional form for  $I^2\chi(\omega)$  and least squares fit a few parameters to the data can also be employed based on the simplified equations described above instead of employing the full Eliashberg equations. For instance, the new equations of Sharapov and Carbotte<sup>38</sup> have already been used in this way by Hwang *et al.*<sup>40</sup> to analyze data in underdoped Ortho-II YBCO<sub>6.5</sub>.

The aim of this paper is to understand better how limitations in accuracy of the simplified formulas can impact on the resulting form of  $I^2\chi(\omega)$  and to explore as well

the advantages and limitations of numerical inversion techniques such as SVD and Maximum Entropy Method (MaxEnt) as well as least squares fit.

The paper is organized as follows. In Sec. II the formal background is discussed. One subsection concentrates on the three major methods of inversion, namely the second derivative method, deconvolution methods based on approximate relations, and the least squares fit method. The second subsection discusses approximate formulas for the normal and superconducting state which allow to calculate the optical scattering rate  $\tau_{op}^{-1}(\omega)$  from a given spectral density  $\alpha^2F(\omega)$  using a convolution integral. Section III discusses numerically the caveats and merits of the various methods of inversion by studying normal metals as well as High- $T_c$  cuprates. Computer generated and experimental  $\tau_{op}^{-1}(\omega)$  data for the normal and superconducting state are used as input for the inversion. Finally, conclusions are drawn in Sec. IV. Two appendices have been added. Appendix A gives an overview of the Maximum Entropy method in terms of Bayesian probability theory. Appendix B presents all important equations which allow to calculate the optical scattering rate within the framework of full Eliashberg theory.

## II. FORMALISM

### A. Methods of Inversion

In order to understand the mechanism of superconductivity it is important to have detailed knowledge of the spectral function  $\alpha^2F(\omega)$  and as tunneling, the established source of information on  $\alpha^2F(\omega)$ ,<sup>5</sup> was initially not a successful tool in the high- $T_c$  superconductors, the infrared optical conductivity became increasingly important, particularly in the form of the optical scattering rate

$$\tau_{op}^{-1}(\omega) = \frac{\Omega_p^2}{4\pi} \Re [\sigma_{op}^{-1}(\omega)] \quad (1)$$

of extended Drude theory. Here,  $\Omega_p$  is the plasma frequency.

There are, in principle, three methods to extract the information on  $\alpha^2F(\omega)$  from the optical scattering rate (inversion). An essential requirement for a solution obtained with any of these methods is that the result should match the data points as well as possible. In order to assess the quality of the fit we need to know how the experimental data points  $t_i \equiv \tau_{ex}^{-1}(\omega_i)$  scatter around the ‘true’ values  $t_i^0 \equiv \tau_{op}^{-1}(\omega_i)$ , that is, we need to know in terms of Bayesian probability theory the likelihood  $p(\mathbf{t}|\mathbf{t}^0, \mathcal{I})$ . It describes the distribution of  $N$  data points  $\mathbf{t} = \{t_i|i = 1, \dots, N\}$  given the ‘exact’ values  $\mathbf{t}^0 = \{t_i^0|i = 1, \dots, N\}$ , which are usually expressed in terms of the parameters of the physical model. The symbol  $\mathcal{I}$  designates all additionally available background information comprising the experimental setup as well as the physical model employed.

The likelihood is determined by the experimental setup and we have to keep in mind that the experimental signal contains at least three contributions<sup>41</sup>

$$\tau_{ex}^{-1}(\omega) = \tau_{op}^{-1}(\omega) + B(\omega) \pm \eta(\omega), \quad (2)$$

with  $B(\omega)$  usually a slowly varying background signal which is typical of the experimental setup and  $\eta(\omega)$ , the noise in the data.

Unfortunately, we do not have any knowledge concerning the functional form of the likelihood for the experimental data sets considered in this study. Therefore, we make the *assumption* of an uncorrelated normal distribution with standard deviation  $\sigma$ :

$$p(\mathbf{t}|\mathbf{t}^0, \mathcal{I}) = (2\pi\sigma^2)^{-N/2} \exp\left(-\frac{1}{2}\gamma^2\right). \quad (3)$$

Here  $\gamma^2$  is the misfit

$$\gamma^2 = \sum_i r_i^2 \quad (4)$$

which is expressed in terms of the residuals

$$r_i = \frac{t_i - t_i^0}{\sigma}. \quad (5)$$

They measure the deviation of the data points  $t_i$  from the ‘true’ values  $t_i^0$  (or the best estimates thereof) in units of the error bar  $\sigma$ .

For lack of further information, we argue that the likelihood (3) is a reasonable choice and we note that it is, in fact, the most uninformative probability distribution given only the mean value and the variance and *no further information*.<sup>41</sup> We want to stress that curve fitting with minimization of the misfit  $\gamma^2$  is also implicitly based on the assumption of a Gaussian likelihood.

The problem of obtaining  $\alpha^2 F(\omega)$  from  $\tau_{ex}^{-1}(\omega)$  is extremely ill conditioned. This implies that a direct solution will be totally dominated by noise and, therefore, be completely meaningless. For this reason, all methods discussed here involve a *nuisance* or regularization parameter that can be tuned in order to suppress noise contributions. Apart from ad-hoc settings, a sensible choice is to adjust the regularization parameter such that  $\gamma^2 = N$  is obtained. (See Appendix A.)

The first method of inversion is based on the relationship<sup>10</sup>

$$W(\omega) = \frac{1}{2\pi} \frac{d^2}{d\omega^2} [\omega \tau_{op}^{-1}(\omega)] \quad (6)$$

which is approximately equal to  $\alpha^2 F(\omega)$  at zero temperature and in the normal state. Application of this formula to experimental data will result in numerical difficulties because we have to keep in mind that the experimental signal  $\tau_{ex}^{-1}(\omega)$  consists, according to Eq. (2), of at least three contributions. Two of these, namely  $B(\omega)$  and  $\eta(\omega)$  can obscure completely the looked for spectral function

$\alpha^2 F(\omega)$  when the second derivative of  $\tau_{ex}^{-1}(\omega)$  is calculated.

On first sight, Eq. (6) would require that  $\tau_{ex}^{-1}(\omega)$  must be ambiguously smoothed ‘by hand’<sup>36</sup> which is certainly not true. First of all, it is much better to ‘smooth’ the function  $\omega \tau_{ex}^{-1}(\omega)$  which is monotonically increasing, much less structured, and equal to zero at  $\omega = 0$ . The application of standard data processing techniques like Fast-Fourier-Transform (FFT) smoothing or FFT low pass filters on this function allows one to remove quite reliably the noise contribution  $\eta(\omega)$ . For instance, the upper frequency threshold applied to the FFT low pass filter will play the role of a nuisance (or renormalization) parameter in this particular case. If there is further knowledge about the background function  $B(\omega)$  application of Eq. (6) is much safer than it looks on first sight. We will discuss caveats and merits of this *second derivative method* later on using computer generated results which ensure  $B(\omega) = 0$  and which allow a controlled noise contribution  $\eta(\omega)$ .

The second method of inversion is based on the deconvolution of the approximate relation

$$\tau_{op}^{-1}(\omega; T) = \int_0^\infty d\Omega K(\omega, \Omega; T) \alpha^2 F(\Omega), \quad (7)$$

where  $T$  denotes the temperature. The kernel  $K(\omega, \Omega; T)$  is determined from theory. The caveat of this method is that solutions of Eq. (7) for  $\alpha^2 F(\omega)$  are not unique because, generally, the deconvolution of Eq. (7) constitutes an ill-posed problem.

There are two approaches to solve this deconvolution problem and both are based on a discretization of Eq. (7) of the form

$$\tau_{op}^{-1}(\omega_i; T) = \sum_{j=1}^{N_2} \Delta\Omega_j K(\omega_i, \Omega_j; T) \alpha^2 F(\Omega_j), \quad (8)$$

with  $i = 1, \dots, N_1$  and  $\Delta\Omega_j = \Omega_{j+1} - \Omega_j$ . The first approach is straight forward and is called *Singular Value Decomposition*<sup>42</sup> (SVD) which is based on the vector form of Eq. (8), namely

$$\mathbf{t} = \mathbf{K} \mathbf{a}, \quad (9)$$

with the vector  $\mathbf{t} = \{t_i = \tau_{op,ex}^{-1}(\omega_i; T) | i = 1, \dots, N_1\}$ , the matrix  $\mathbf{K} = \{K_{ij} = \Delta\Omega_j K(\omega_i, \Omega_j; T) | i = 1, \dots, N_1, j = 1, \dots, N_2\}$ , and the vector  $\mathbf{a} = \{a_j = \alpha^2 F(\Omega_j) | j = 1, \dots, N_2\}$ . Using SVD, the matrix  $\mathbf{K}$  of dimension  $N_1 \times N_2$  is transformed into the matrix product  $\mathbf{U} \mathbf{S} \mathbf{V}^T$ , with  $\mathbf{U}$  and  $\mathbf{V}$  being unitary matrices of dimension  $N_1 \times N_2$  and  $N_2 \times N_2$  respectively. The matrix  $\mathbf{S} = \text{diag}\{s_j | j = 1, \dots, N_2\}$  with  $s_j$  the singular values (svs). Finally,  $\mathbf{V}^T$  denotes the transposed matrix  $\mathbf{V}$ . If the vector  $\mathbf{t}$  and the matrix  $\mathbf{K}$  are known the vector  $\mathbf{a}$  and, thus,  $\alpha^2 F(\omega)$  can be determined by ‘inverting’ Eq. (9):  $\mathbf{a} = \mathbf{V} \mathbf{S}' \mathbf{U}^T \mathbf{t}$  with  $\mathbf{S}' = \text{diag}\{1/s_j | j = 1, \dots, N_2\}$ . However, noise contained in the data  $\mathbf{t}$  will be dramatically

magnified by smallest svcs, rendering the result meaningless. For this reason, all contributions by svcs below a certain threshold have to be discarded by replacing the corresponding diagonal elements  $1/s_i$  in the matrix  $\mathbf{S}'$  by zeros. This threshold plays the role of the nuisance parameter in the SVD method. Dordevic *et al.*<sup>36</sup> studied this approach extensively and discussed in particular the number of svcs necessary to get a ‘smooth’ spectral function  $\alpha^2 F(\omega)$  together with a reasonable reconstruction of the input data. In principle the problem of ‘smoothing by hand’ is moved from the input to the output of the process. The caveat of this approach is the fact that it doesn’t ensure that the resulting spectral function  $\alpha^2 F(\omega)$  be positive definite. Most of the time,  $\alpha^2 F(\omega)$  will contain negative parts which cannot be removed even by applying further regularization schemes.<sup>36</sup> Such negative parts are unphysical.

The second approach to the deconvolution problem is the so-called *Maximum Entropy Method* (MaxEnt). Originally, E.T. Jaynes<sup>43</sup> suggested the Maximum Entropy principle for the assignment of probability distributions: If only some testable information such as the mean value is given, one should select that probability distribution  $\{p_i\}$  which maximizes the Shannon entropy<sup>41</sup>  $S = -\sum_{i=1}^N p_i \log(p_i)$  subject to all known constraints. In the case where only the mean and the variance are known, the normal distribution is the ‘most uninformative’ probability distribution (pdf). Although the ‘true’ pdf may be completely different, a normal distribution can be a sensible choice for lack of further background information.

The MaxEnt principle has been generalized to the inference of strictly positive functions such as the spectral function  $\alpha^2 F(\omega)$  within Bayesian probability theory. This fully probabilistic description allows for an explicit treatment of the ambiguity inherent in badly conditioned problems and is discussed in some detail in Appendix A. In our particular case the generalized Shannon-Jaynes entropy (A3) is applicable with the default model vector  $\mathbf{m}$  chosen to be constant.

The third method of inversion uses model spectral functions which depend on a few parameters which are then determined using a *least squares fit* to experiment based either on approximate formulas of the form (7) or full Eliashberg theory. Very often preliminary results derived with the help of the second derivative method from experiment (or using one of the other above mentioned methods) can be utilized to minimize the number of parameters to be fitted. Results from other experiments, for instance inelastic neutron scattering etc., can easily be incorporated. Nevertheless, in general this method will also result in non-unique solutions for  $\alpha^2 F(\omega)$ .

## B. Approximate Formulas

For the normal state at zero temperature Allen<sup>3</sup> provided a simplified form of the kernel of Eq. (7), namely

$$K(\omega, \Omega; T = 0) = \frac{2\pi}{\omega} (\omega - \Omega) \theta(\omega - \Omega), \quad (10)$$

where  $\theta(x)$  is the step function. This formula is based on a second order perturbation theory approach based on the weak electron-phonon coupling in normal metals. To overcome the zero temperature restriction Shulga *et al.*<sup>37</sup> started from a full Eliashberg description of the electron-phonon formalism and applied a series of approximations to reduce the full results to the approximate form

$$K(\omega, \Omega; T) = \frac{\pi}{\omega} \left[ 2\omega \coth\left(\frac{\Omega}{2T}\right) - (\omega + \Omega) \coth\left(\frac{\omega + \Omega}{2T}\right) + (\omega - \Omega) \coth\left(\frac{\omega - \Omega}{2T}\right) \right], \quad (11)$$

which properly reduces to Eq. (10) for  $T = 0$ . When applied to invert data one has to keep in mind that this kernel becomes singular for  $\Omega = 0$ .

The work of Shulga *et al.* was generalized recently by Sharapov and Carbotte<sup>38</sup> to treat the possibility of a pseudogap opening up in the fully dressed density of states  $\tilde{N}(\omega)$ . They obtain

$$K(\omega, \Omega; T) = \frac{\pi}{\omega} \int_{-\infty}^{\infty} d\varepsilon \left[ \frac{\tilde{N}(\varepsilon - \Omega)}{N(0)} + \frac{\tilde{N}(\Omega - \varepsilon)}{N(0)} \right] \times [n(\Omega; T) + f(\Omega - \varepsilon; T)] [f(\varepsilon - \omega; T) - f(\varepsilon + \omega; T)], \quad (12)$$

which properly reduces to the result (11) of Shulga *et al.*<sup>37</sup> when  $\tilde{N}(\omega)$  is taken to be constant and equal to  $N(0)$ . Here  $n(\omega; T)$  and  $f(\omega; T)$  are the Bose and Fermi distributions, respectively. The zero temperature limit of Eq. (12) was obtained by Mitrović and Fiorucci<sup>8</sup> based on Allen’s second order perturbation theory approach.

Allen also provided a kernel similar to Eq. (10) which applies approximately in the superconducting state at zero temperature. In this case the kernel is of the form

$$K(\omega, \Omega; T = 0) = \frac{2\pi}{\omega} (\omega - \Omega) \theta(\omega + 2\Delta_0 - \Omega) \times E\left(\sqrt{1 - \frac{4\Delta_0^2}{(\omega - \Omega)^2}}\right). \quad (13)$$

It ensures that  $\tau_{op}^{-1}(\omega)$  is zero for  $0 \leq \omega \leq 2\Delta_0$ . Here,  $E(x)$  is the complete elliptic integral of the second kind and  $\Delta_0$  is the energy gap at  $T = 0$ . To derive Eq. (13) Allen treated the superconducting transition within the framework of BCS theory, i.e.: Eq. (13) is only valid for *s*-wave symmetry of the superconducting order parameter. Moreover,  $\Delta_0$  is an external parameter to Eq. (13) and its value has to be determined by other means. Treating the superconducting transition within the framework of Eliashberg theory will certainly go beyond the possibilities of Eq. (13) and this will have to be kept in mind when

Eq. (13) is applied to invert superconducting state optical data of real *s*-wave superconductors which are well known to be exceptionally well described by Eliashberg theory.<sup>2</sup>

A consensus exists that in the high  $T_c$  cuprates the superconducting order parameter is of *d*-wave rather than *s*-wave symmetry. It was pointed out by Carbotte and Schachinger<sup>39</sup> that it is a simple matter to generalize the second order perturbation theory calculations of Allen to include *d*-wave symmetry. The result is that Eq. (13) needs to be averaged over the polar angle  $\vartheta$  of the two dimensional  $\text{CuO}_2$  Brillouin zone. This results in the kernel

$$K(\omega, \Omega; T=0) = \frac{2\pi}{\omega} \langle (\omega - \Omega)\theta(\omega + 2\Delta_0(\vartheta) - \Omega) \times E \left( \sqrt{1 - \frac{4\Delta_0^2(\vartheta)}{(\omega - \Omega)^2}} \right) \rangle_{\vartheta}, \quad (14)$$

with  $\langle \dots \rangle_{\vartheta}$  denoting the  $\vartheta$ -average which can be limited to the interval  $\vartheta \in [0, \pi/4]$  for symmetry reasons. Furthermore,  $\Delta_0(\vartheta) = \Delta_0 \cos(2\vartheta)$  reflecting the *d*-wave symmetry of the superconducting order parameter. Eq. (14) ensures that the optical scattering rate is finite in the superconducting state for  $\omega > 0$ . This is in contrast to what is observed in *s*-wave superconductors.

### III. NUMERICAL RESULTS

#### A. Normal Metals

We will study in quite some detail the various inversion techniques using, as a first material, lead. The electron-phonon spectral density  $\alpha^2 F(\omega)$  was derived from tunneling data by McMillan and Rowell.<sup>5</sup> This spectrum, which is shown in the top frame of Fig. 1 as gray solid squares, has two distinctive peaks which are separated from each other by about 4 meV. The Debye energy  $\omega_D = 11.2 \text{ meV}$ . Optical data for lead was obtained by Joyce and Richards<sup>44</sup> and later by Farnworth and Timusk.<sup>6</sup> The extracted  $\alpha^2 F_{tr}(\omega)$  was found to be in remarkable good agreement with earlier tunneling data and with the results of direct band structure calculations of  $\alpha^2 F(\omega)$  by Tomlinson and Carbotte.<sup>7</sup> Here this spectrum will be used to generate optical scattering rate data using the various kernels discussed in Sec. IIB as well as with the complete Eliashberg equations of Appendix B.

In a first step zero temperature, normal state data are generated using kernel (10). We calculate the function  $W(\omega)$  (dotted line, upper frame Fig. 1) using the second derivative method and the agreement with the input spectrum (gray solid squares) is almost perfect without the need of ‘smoothing by hand’. (Only the second peak shows oscillations.) Inversion of the input data using the SVD method results in the curve  $\text{SVD}(\omega)$  (dashed line, upper frame Fig. 1). The svcs threshold was set to  $10^{-3}$ , i.e.: 87 svcs have been used. A few wiggles remain in the

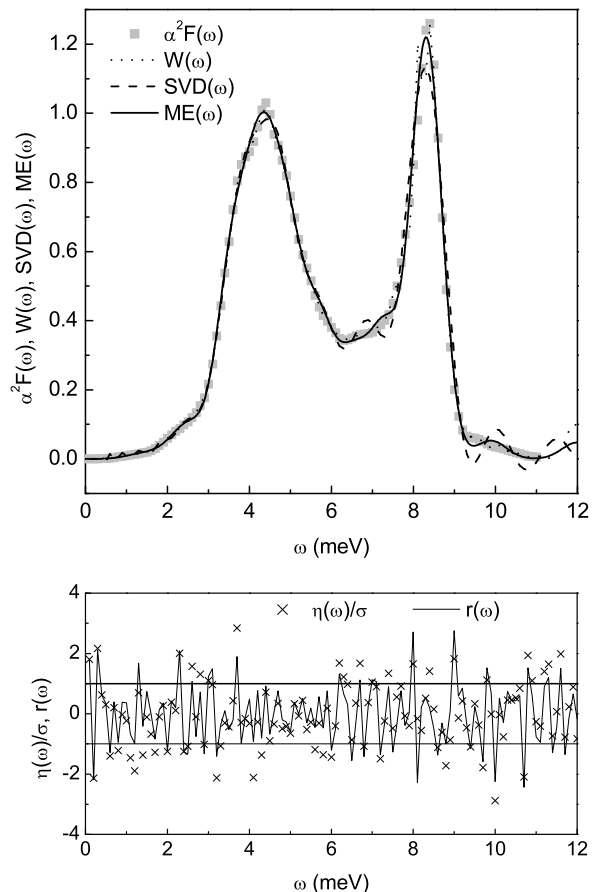


FIG. 1: Top frame: Inversion of zero temperature, normal state optical scattering rate data  $\tau_{op}^{-1}(\omega)$  of lead generated using the kernel (10). The gray solid squares indicate the  $\alpha^2 F(\omega)$  used to generate the data. The dotted line corresponds to the function  $W(\omega)$  according to Eq. (6),  $\text{SVD}(\omega)$  (dashed line) shows the result of an SVD inversion, and  $\text{ME}(\omega)$  (solid line) presents the result of a MaxEnt inversion. Bottom frame: The crosses correspond to the normalized uncorrelated Gaussian noise  $\eta(\omega)/\sigma$  which was added to the input data for the MaxEnt inversion and  $r(\omega)$  (solid line) gives the residual of the MaxEnt data reconstruction.

valley between the two peaks and we see oscillations at energies  $> 10 \text{ meV}$  which also go negative. Data beyond the Debye energy are irrelevant.

For the application of the MaxEnt method we add uncorrelated Gaussian noise of standard deviation  $\sigma = 10^{-3}$  to ensure a controlled error distribution for the input data. (This, in principle, biases the comparison in favour of the second derivative and SVD method.) The curve  $\text{ME}(\omega)$  (solid line, upper frame Fig. 1 presents the result of the MaxEnt inversion in which we used optimized preblur [blur-width  $b = 0.05$ , see Eq. (A4)] and the default model was set to  $m_j = 0.001$ .  $\text{ME}(\omega)$  underestimates slightly the second peak but otherwise shows perfect agreement with the input spectrum. We also see

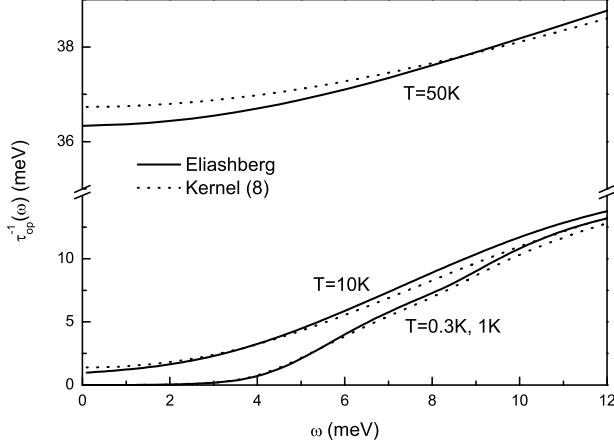


FIG. 2: Temperature dependence of the normal state optical scattering rate  $\tau_{op}^{-1}(\omega)$  of lead. The solid lines correspond to results derived using Eliashberg theory and the dashed lines correspond to data generated using kernel (11). Temperatures are 0.3 K, 1 K, 10 K, and 50 K.

an additional feature beyond the Debye energy which is irrelevant because it reflects the default model. The bottom frame of Fig. 1 demonstrates the quality of the data reconstruction achieved by the MaxEnt method. The crosses symbolize the normalized noise  $\eta(\omega)\sigma$  which was added to the optical scattering rate and the solid line corresponds to the residual (5). As we only added noise to the computer generated  $\tau_{op}^{-1}(\omega)$ ,  $r(\omega)$  should track the normalized noise  $\eta(\omega)/\sigma$ , as it does.

Zero temperature is not a realistic case and we proceed in studying normal state, finite temperature results. There are two options to generate optical scattering rate data: (a) kernel (11) is applied, or (b) Eliashberg theory (see Appendix B) is used. The superconducting order parameter is zero in the normal state and the renormalization formula (B1b) takes on a closed form. Fig. 2 presents our results for the temperature dependence of the optical scattering rate in lead for four different temperatures, namely 0.3 K, 1 K, 10 K, and 50 K. The results according to Eliashberg theory are presented by solid lines, while the dashed lines correspond to the results of kernel (11). There are small but distinct differences between the two sets of data.

Fig. 3 presents the spectra  $W(\omega)$ ,  $SVD(\omega)$ , and  $ME(\omega)$  which result from the application of the first two methods of inversion discussed in Sec. II A. As input we used the finite temperature normal state optical scattering rate for lead generated using kernel (11) (dashed lines of Fig. 2). The top frame presents as a result of the second derivative method, the function  $W(\omega)$  as defined in Eq. (6). At the lowest temperature,  $T = 0.3$  K the input  $\alpha^2 F(\omega)$  (grey solid squares) is perfectly reproduced (solid line), while at  $T = 1$  K (dashed line) the high energy peak is already

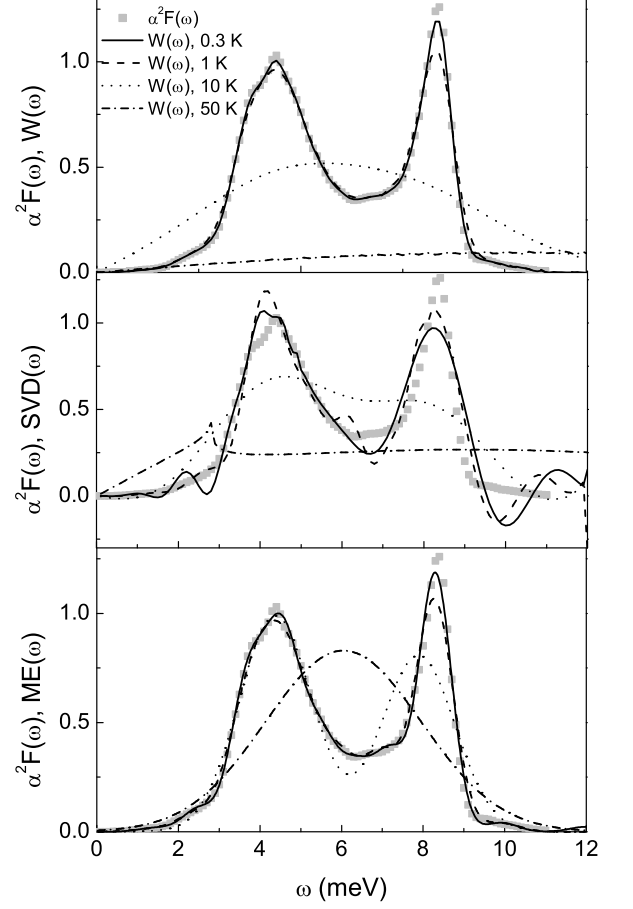


FIG. 3: Inversion of finite temperature, normal state optical scattering rates generated from kernel (11). The solid lines correspond to the temperature  $T = 0.3$  K, dashed lines to 1 K, dotted lines to 10 K, and dash-dotted lines to 50 K. The gray solid squares represent the  $\alpha^2 F(\omega)$  spectral function applied to calculate the optical scattering rate data. Top frame: Second derivative method. Center frame: SVD method. Bottom frame: MaxEnt method.

underestimated. At  $T = 10$  K (dotted line) the method is not longer able to resolve the two peak structure, and at  $T = 50$  K (dash-dotted) line the method fails completely. Nevertheless, it has to be emphasized that no smoothing had to be applied to the input data as no artificial noise had been added.

The center frame of Fig. 3 presents the results  $SVD(\omega)$  of a singular value decomposition of Eq. (9) using kernel (11). The svcs threshold was set to  $10^{-3}$ . At  $T = 0.3$  K and 1 K we obtain reasonable agreement with the  $\alpha^2 F(\omega)$ . For energies  $> 9$  meV the inversion shows oscillations and  $SVD(\omega)$  even becomes negative which is unphysical. We also see oscillations at low energies and between the two peaks. At  $T = 10$  K the SVD method still resolves a hint of a two peak structure in contrast to

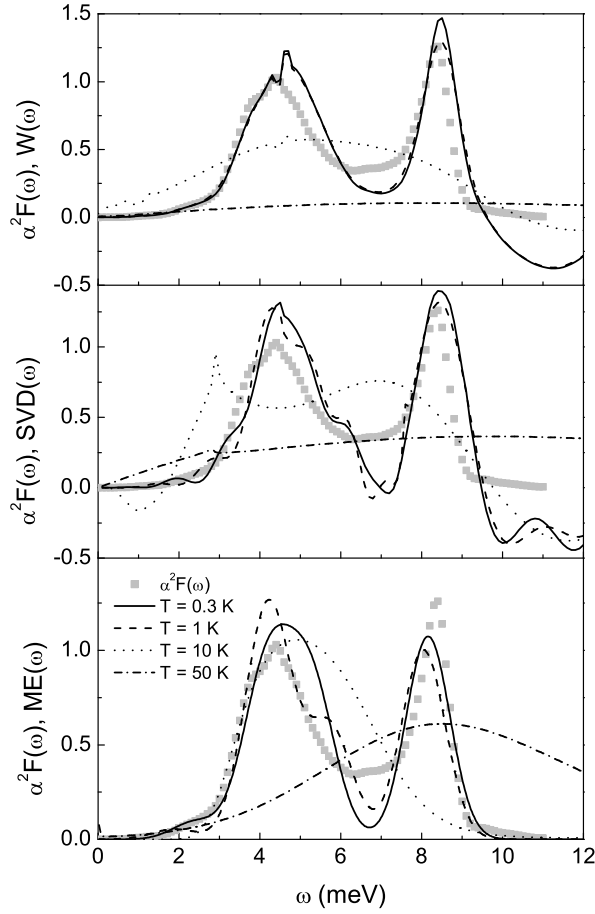


FIG. 4: The same as Fig. 3 but now the Eliashberg theory generated normal state, finite temperature optical scattering rates (solid lines in Fig. 2) are used as input.

the second derivative method. Finally, at  $T = 50$  K the method fails completely.

The bottom frame of Fig. 3 presents the results  $ME(\omega)$  of the MaxEnt deconvolution of Eq. (8). Uncorrelated Gaussian noise of  $\sigma = 10^{-3}$  was added to the computer generated data. For the inversion optimized preblur (see Appendix A) was applied with  $b = 0.4$  for  $T = 0.3$  K,  $b = 0.46$  for 1 K,  $b = 0.89$  for  $T = 10$  K, and  $b = 1.91$  for  $T = 50$  K. The default model was set to  $m_j = 0.01$ . The  $T = 0.3$  K inversion (solid line) gives almost perfect agreement with the model  $\alpha^2 F(\omega)$  spectral function. At  $T = 1$  K the high energy peak is underestimated but reproduced at the appropriate energy. At  $T = 10$  K, the two peak structure is still well resolved, only the second peak is underestimated and shifted to lower energies. The result is certainly much better than that of the other two methods. Finally, at  $T = 50$  K MaxEnt is no longer able to resolve the two peak structure. Nevertheless, it is quite interesting to note that the area under the dash-dotted curve is 3.95 meV which is very close to the area 4.03 meV under the original  $\alpha^2 F(\omega)$  spectral function.

Fig. 2 demonstrated that optical scattering rates generated from full normal state Eliashberg theory differ from the approximate results of kernel (11). It can also be assumed that real metals will more likely follow the predictions of full Eliashberg theory rather than approximate model equations. It is therefore interesting to investigate how the inversion on the basis of the approximate kernel (11) performs when optical scattering rates generated by full Eliashberg theory are used as input. The result is presented in Fig. 4 which is organized the same way as Fig. 3. The top frame demonstrates the application of the second derivative formula which shouldn't have any problems because this method is not based on approximate models formulas. Nevertheless,  $W(\omega)$  is only in reasonable agreement with the original  $\alpha^2 F(\omega)$  at low temperatures. The low energy peak is overestimated and shifted towards higher energies, the valley between the peaks is too low, the second peak is positioned at the correct energy but its height is over/underestimated. At  $T = 10$  K the two peak structure is not any longer resolved and at  $T = 50$  K inversion fails. The central frame of Fig. 4 presents the function  $SVD(\omega)$  as a result of an SVD inversion. The sv threshold was set at  $10^{-2}$ . At low temperatures, the peak positions are at the proper energies, nevertheless the low energy peak is overestimated, the valley between the peaks underestimated, and the high energy peak is too wide. At  $T = 10$  K a two peak structure is resolved but both peaks are placed at the wrong energies. At  $T = 50$  K the method fails altogether. It is typical for this method to show oscillations at energies  $> 9$  meV which result in unphysical negative contributions even at energies below  $\omega_D$ .

Before applying the MaxEnt inversion uncorrelated Gaussian noise of  $\sigma = 0.1$  was added to the input data. For the temperature 0.3 K and 1 K the preblur parameter was optimized to 0.54 at higher temperatures no preblur has been applied. The default model was set to 0.01. At low temperatures MaxEnt overestimates the low energy peak and/or makes it broader. The valley between the peaks is too low, the second peak is resolved reasonably well and is at the proper position but underestimated in height. At higher temperatures the two peak structure is not longer resolved ( $T = 10$  K, dotted line and  $T = 50$  K, dash-dotted line). Nevertheless, data reconstruction is within error bars and this proves that we face in this case a deconvolution problem which is particularly ill conditioned.

All this demonstrates quite clearly that the application of methods of inversion based on approximate models to real material data can quite easily result in deconvoluted spectra  $\alpha^2 F(\omega)$  which will be close but not necessarily equal to the real electron-phonon spectrum which governs the interaction. In particular, the deviations from the gray solid squares in the central and bottom frame of Fig. 4 represent the deviations from the 'real'  $\alpha^2 F(\omega)$  required by the approximate kernels to reproduce the input optical scattering rate data as good as possible.

We now move on to a discussion of superconducting

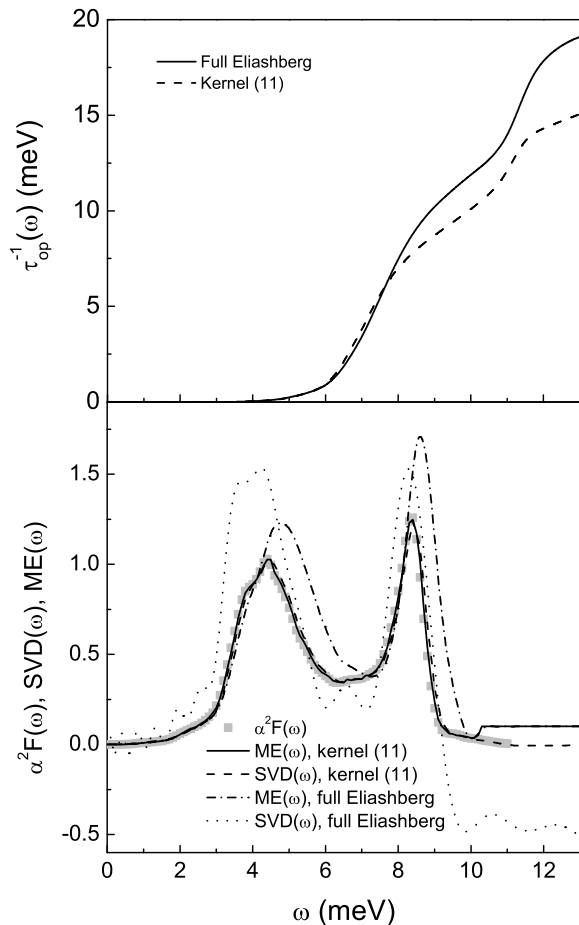


FIG. 5: Top frame: The superconducting state optical scattering rate  $\tau_{op}^{-1}(\omega)$  for Pb at  $T = 0.05T_c$  with  $T_c = 7.2K$ . The solid line is based on the full Eqs. (B1) while the dashed line is obtained using the simplified kernel (13). Bottom frame: The gray squares symbolize the  $\alpha^2 F(\omega)$  of Pb. The solid line is the result of the inversion of the dashed line in the top frame using the MaxEnt method while the dashed line corresponds to an SVD inversion. The dash-dotted and dotted lines present equivalent results but now for full Eliashberg data (solid line in the top frame).

state data. The top frame of Fig. 5 presents the results for the superconducting state optical scattering rate  $\tau_{op}^{-1}(\omega)$  in Pb at  $T = 0.05T_c$  with  $T_c = 7.2K$ . The solid line was obtained on evaluation of the full Eqs. (B1) and (B2) taken for  $s$ -wave symmetry of the superconducting order parameter and a Coulomb pseudopotential  $\mu^* = 0.1438$ . The dashed line is for comparison and was obtained from kernel (13) using the electron-phonon spectral density  $\alpha^2 F(\omega)$  shown as gray solid squares in the bottom frame of this figure. The approximate kernel (13) is evaluated with  $\Delta_0 = 1.39\text{ meV}$ , the gap edge predicted by the full Eliashberg calculation.

The bottom frame of Fig. 5 presents the result of SVD as well as MaxEnt inversions based on the approximate

kernel (13). The dashed line corresponds to the SVD inversion (svs threshold was set to  $10^{-2}$ ) of the optical scattering rate generated using kernel (13) (dashed line in the top frame of Fig. 8).  $\Delta_0$  has been set to  $1.39\text{ meV}$ . As expected, the agreement is almost perfect. The dotted line, on the other hand, shows the result of an SVD inversion of full Eliashberg data (solid line in the top frame). Here, the lower, transverse peak centered around  $\sim 4\text{ meV}$  is broader and the area under the peak is larger. The same holds for the upper, longitudinal phonon peak but the differences are now less pronounced. Beyond  $\sim 9\text{ meV}$  the dotted line becomes negative giving unphysical results.

The MaxEnt inversion was performed by attaching error bars of  $\sigma = 10^{-2}$  to the data and by adding uncorrelated Gaussian noise of the same  $\sigma$ . Furthermore, no plebur was applied and the default model was set to 0.1. The solid line is the MaxEnt inversion of the data generated with the help of kernel (13) (dashed line in the top frame of Fig. 5). Again we achieve perfect agreement. At energies  $> 10.5\text{ meV}$  the function  $ME(\omega)$  levels off at the value 0.1 demonstrating the influence of the chosen default model. The dash-dotted curve, on the other hand, is based on full Eliashberg theory generated input data (solid line in the top frame of this figure). Both peaks are now overestimated in their height and width and both peaks are shifted towards higher energies. Nevertheless,  $ME(\omega)$  never becomes negative which proves that there exists a positive definite solution for the deconvolution problem of Eq. (7). As real data are more likely to be close to the full Eliashberg theory results, the deconvolution of Eq. (7) on the basis of kernel (13) will result in an electron-phonon spectral density  $\alpha^2 F(\omega)$  which will not agree in all details with the real spectral density despite the fact that the input data will be excellently reproduced. The only possible check for the validity of the deconvoluted electron-phonon spectral density  $SVD(\omega)$  or  $ME(\omega)$  is in using it to calculate the optical scattering rate using full Eliashberg theory and compare with the data. Such a comparison will then result in the necessary readjustments of the deconvoluted spectrum.

## B. High- $T_c$ cuprates

In contrast to the normal metal lead, the high  $T_c$  cuprates are not likely to be an electron-phonon system, they are known to be highly correlated systems. There is a class of models used to describe such systems and we will refer to these systems as boson exchange models. They have many common elements with the electron-phonon case. In particular, there exists a well developed literature on the Nearly Antiferromagnetic Fermi Liquid model (NAFFL) introduced by Pines and collaborators.<sup>11,12</sup> The exchange bosons are antiferromagnetic spin fluctuations as described by Millis *et al.*<sup>33</sup> (MMP). Within this model the Eliashberg equations are retained but the boson spectral density is replaced by



the imaginary part of the spin susceptibility multiplied by the square of a coupling of the spin fluctuations to the charge carriers. In general, this interaction is anisotropic and not pinned to the Fermi surface.<sup>45</sup> Nevertheless, as a first approximation, one can work with a simple interaction spectral function  $I^2\chi(\omega)$  which replaces the  $\alpha^2F(\omega)$  of Eliashberg theory. Carbotte *et al.*<sup>29</sup> found that in optimally doped, twinned YBCO single crystals the measured optical scattering rate  $\tau_{ex}^{-1}(\omega)$ , reported by Basov *et al.*<sup>46</sup>, can be well described by a single MMP form:

$$I^2\chi(\omega) = I^2 \frac{\omega/\omega_{SF}}{1 + (\omega/\omega_{SF})^2}. \quad (15)$$

The two parameters, the square of the coupling constant  $I$  and the characteristic spin fluctuation energy  $\omega_{SF}$  were determined from a least squares fit to the data in the energy interval  $0 \leq \omega \leq 250$  meV. The values  $I^2 = 0.83$  and  $\omega_{SF} = 20$  meV have been reported.

Based on the results for lead we cannot necessarily expect inversions of  $\tau_{op}^{-1}(\omega)$  measured around  $T = 100$  K or even higher will be feasible. To investigate this, normal state optical scattering rates are calculated at various temperatures, namely  $T = 1$  K, 10 K, 50 K, and 100 K using either kernel (11) or full Eliashberg theory with an  $I^2\chi(\omega)$  determined by Eq. (15) and parameters  $I^2$  and  $\omega_{SF}$  as reported by CSB. The results of the inversion based on the approximate kernel (11) are discussed in Fig. 6 with input data  $\tau_{ex}^{-1}(\omega)$  generated using kernel (11) and, in Fig. 7 with  $\tau_{ex}^{-1}(\omega)$  generated by full Eliashberg theory.

The top frame of Fig. 6 presents results for  $W(\omega)$  from the second derivative method. At the two lowest temperatures, namely  $T = 1$  K (solid line) and 10 K (dashed line) the  $I^2\chi(\omega)$  spectrum (gray solid squares) is almost perfectly reproduced. At higher temperatures, namely at  $T = 50$  K (dotted line) and 100 K (dash-dotted line) the inverted spectrum develops a less pronounced peak which is also shifted towards higher energies. In the tail ( $\omega > 100$  meV) noise develops in the inverted spectrum. Nevertheless, in contrast to lead with its narrow two peak structure the simple MMP form can easily be inverted from optical scattering rate data even at temperatures around 100 K.

The center frame of Fig. 6 presents the results SVD( $\omega$ ) of a singular value decomposition. The svs threshold was set at  $10^{-3}$  for  $T = 1$  K and 10 K and was increased to  $10^{-2}$  for  $T = 50$  K and 100 K. The inverted spectrum agrees reasonably well with the original spectrum at low energies,  $\omega < 75$  meV. At higher energies pronounced oscillations occur.

The bottom frame of Fig. 6 presents the results ME( $\omega$ ) of a MaxEnt deconvolution. The error bars on the data were determined by  $\sigma = 0.15$  and uncorrelated Gaussian noise of the same  $\sigma$  was added. No preblur was applied. The agreement with the original  $I^2\chi(\omega)$  spectral function (gray squares) is excellent up to temperatures of 50 K. At 100 K the peak at 20 meV is poorly resolved, otherwise the agreement is still rather good.

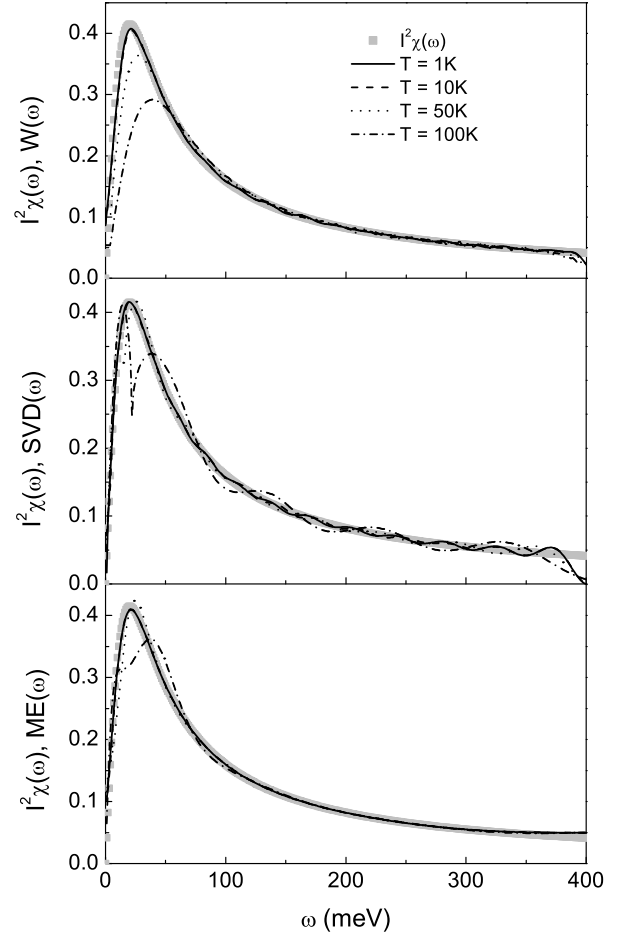


FIG. 6: The same as Fig. 3 with the  $\alpha^2F(\omega)$  replaced by the  $I^2\chi(\omega)$  defined by Eq. (15) with  $I^2 = 0.83$  and  $\omega_{SF} = 20$  meV. The solid lines corresponds to  $T = 1$  K, the dashed lines to 10 K, the dotted lines to 50 K, and the dash-dotted lines to 100 K.

The results presented in Fig. 7 are very similar to the ones shown in Fig. 6 with the difference that SVD and MaxEnt (error bars were determined by  $\sigma = 0.2$ , uncorrelated Gaussian noise of the same  $\sigma$  was added, no preblur) now overestimate the peak at 20 meV. This is the result of minor differences between the optical scattering rates calculated from kernel (11) and full Eliashberg theory. The top frame of Fig. 8 demonstrates how little these differences are.

We proceed by studying the MaxEnt inversion of experimental data and make use of the  $T = 95$  K normal state optical scattering rate measured by Basov *et al.*<sup>46</sup> on an optimally doped, twinned YBCO single crystal. Fig. 8 presents the result of a MaxEnt inversion. We assume the experimental data  $\tau_{ex}^{-1}(\omega)$  to be contaminated by a substantial uncorrelated Gaussian noise of  $\sigma = 2.5$ . The inversion is performed on the basis of kernel (11) and the resulting spectral function ME( $\omega$ ) is shown as a solid line in the middle frame of Fig. 8. ME( $\omega$ ) then

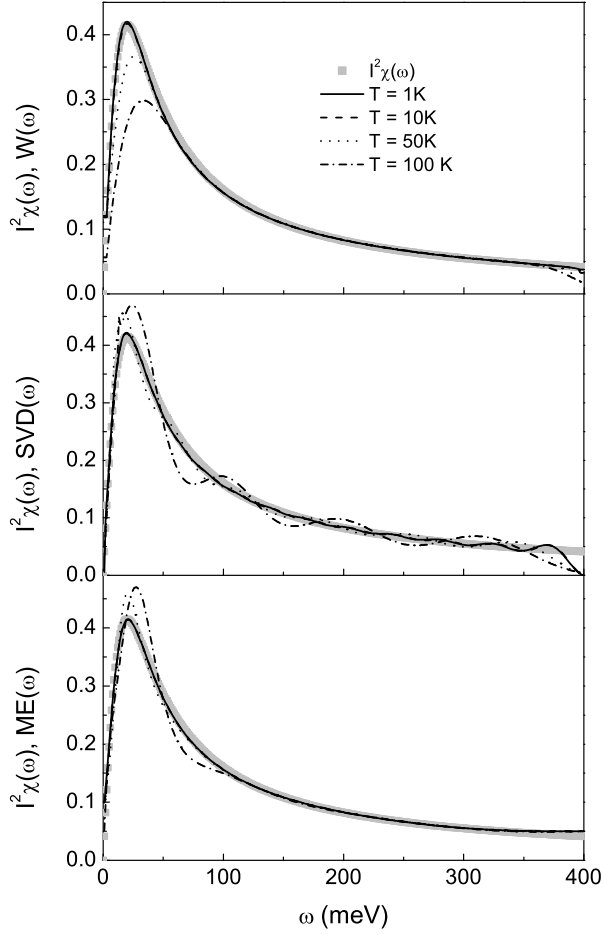


FIG. 7: The same as Fig. 6 but now Eliashberg theory generated optical scattering rates have been used as input for the inversion.

replaces  $\alpha^2 F(\omega)$  in Eq. (7) which is used to calculate the reconstructed optical scattering rate shown by a solid line in the top frame of Fig. 8. It reproduces excellently the input data (gray solid line). For comparison, the top frame of this figure contains two more results, namely the optical scattering rate calculated from full Eliashberg theory (dashed line) using the  $I^2\chi(\omega)$  reported by CSB (gray solid squares in the center frame of Fig. 8). The dotted line, on the other hand, corresponds to  $\tau_{op}^{-1}(\omega)$  calculated from Eq. (7) using kernel (11) and the same  $I^2\chi(\omega)$ . Obviously, the two results are very close with the dotted line slightly above the dashed one at low energies. The opposite holds for high energies. This is in agreement with the result found for lead (see Fig. 2).

Finally, the bottom frame of Fig. 8 shows the residual  $r(\omega)$  which is a measure for the quality of the data reconstruction. Apart from the low energy region the reconstruction is within the assumed standard deviation (indicated by the two straight lines at 1 and -1) of  $\sigma = 2.5$ . The result is to be compared with the  $r(\omega)$  shown in the

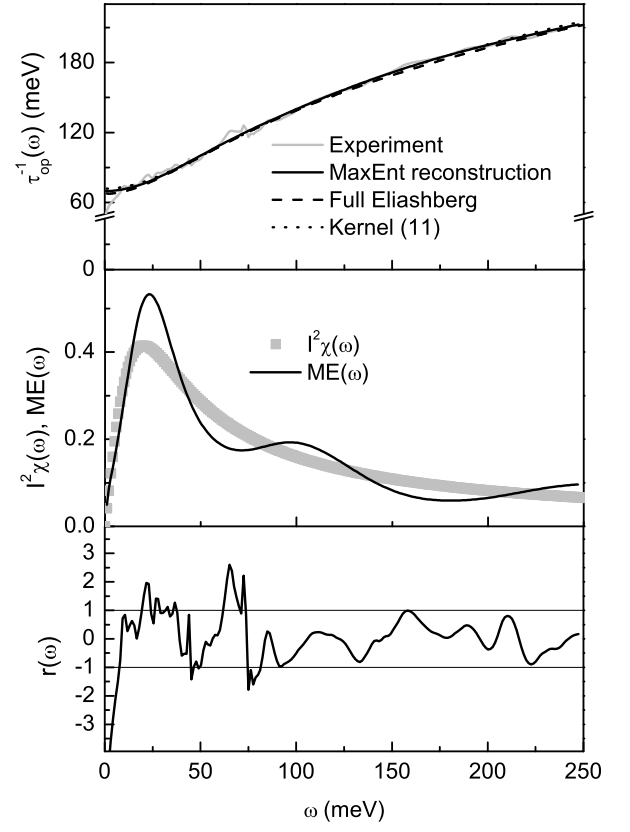


FIG. 8: Top frame: The normal state optical scattering rate  $\tau_{ex}^{-1}(\omega)$  at  $T = 95$  K for an optimally doped, twinned YBCO single crystal. The gray solid line gives the experimental data by Basov *et al.*<sup>46</sup> The solid line corresponds to the MaxEnt reconstruction based on kernel (11) using the spectral function  $ME(\omega)$  shown in the middle frame of this figure (solid line). The dashed line presents the results of a full Eliashberg calculation based on the spectral function  $I^2F(\omega)$  shown as gray solid squares in the middle frame of this figure. Bottom frame: The residual  $r(\omega)$  according to Eq. (14) of the MaxEnt data reconstruction.

bottom frame of Fig. 1 which results from the reconstruction of computer generated data with additional uncorrelated Gaussian noise. The  $r(\omega)$  in the bottom frame of Fig. 8 is a rather smooth function which contains for energies  $> 70$  meV very little stochastic elements which could be identified as noise. The various data points appear to be rather correlated an effect which could either be attributed to an additional background function  $B(\omega)$  [see Eq. (2)] or to a ‘real’ signal. Nevertheless, what is important here is the fact that the inverted  $ME(\omega)$  has a nonzero contribution even at energies  $\sim 250$  meV thus establishing a high energy background in  $I^2\chi(\omega)$  as predicted by CSB. Finally, as both spectral functions presented in the central frame of Fig. 8 reconstruct the input data equally well, both spectral functions can be used as valid spectral functions because of the non-uniqueness of the deconvolution problem. Further calculations and

comparison with other experiments than optical conductivity may then help to discriminate between these two solutions. It is interesting to point out that the area under  $I^2\chi(\omega)$  (42 meV) is approximately reproduced by the area under the spectrum  $ME(\omega)$  (41.4 meV).

Tu *et al.*<sup>30</sup> measured the optical scattering rate of optimally doped  $\text{Bi}_2\text{Sr}_2\text{CaCu}_2\text{O}_{8+\delta}$  (Bi2212) single crystals at various temperatures. They derived, using data analysis different from the methods discussed here, that even in the normal state at 100 K a resonance peak is seen in the function  $W(\omega)$  while it is rather featureless at 295 K. Schachinger and Carbotte<sup>35</sup> also analyzed these data using a combination of the second derivative method and least squares fits to the data. In particular, they found that the  $T = 295$  K data are well described by an MMP form (15) in the energy region  $0 \leq \omega \leq 250$  meV. The least squares fit determined the parameters  $I^2 = 0.655$  and  $\omega_{SF} = 82$  meV using full Eliashberg theory in the fitting procedure.

As MaxEnt turned out to be a rather powerful inversion technique we revisit the Bi2212 data analysis. We assume the experimental data of Tu *et al.* to contain uncorrelated Gaussian noise of  $\sigma = 2.0$  for  $T = 100$  K and  $\sigma = 3.0$  for  $T = 200$  K and 295 K. The preblur parameter was set to 5 for  $T = 100$  K and to 10 for the other two temperatures. The default model was set to 0.1. The inversion is based on the application of the approximate kernel (11). Fig. 9 discusses the results of our calculations. The top frame presents the data reconstruction and the bottom frame the inverted spectral function  $ME(\omega)$  in comparison to  $I^2\chi(\omega)$  spectral functions suggested by Schachinger and Carbotte.<sup>35</sup> It is quite clear that the data reconstruction (solid lines in the top frame of Fig. 9) is in excellent agreement with the original data (gray solid lines) at all temperatures. The dotted lines correspond to  $\tau_{op}^{-1}(\omega)$  data generated from full Eliashberg theory using the  $I^2\chi(\omega)$  spectral functions presented in the bottom frame of Fig. 9 by gray solid symbols, namely diamonds for 100 K, up-triangles for 200 K, and squares for 295 K. The full Eliashberg result follows the data rather nicely in the energy range  $0 \leq \omega \leq 250$  meV and then deviates to smaller values in a pronounced way for energies  $> 250$  meV.

Comparing the spectral functions  $ME(\omega)$  to the  $I^2\chi(\omega)$  spectra demonstrates rather good agreement at low energies for  $T = 100$  K (dotted line, gray solid diamonds). Both spectra show a pronounced peak at 43 meV and they even agree in height and width of the peak which is rather fortuitous. At  $T = 200$  K (dashed line, gray solid up-triangles) both spectra develop a less pronounced peak with the peak in  $ME(\omega)$  shifted away from 43 meV to higher energies. Such a shift towards higher energies with increasing temperatures has already been observed in the analysis of computer generated data and this peak in the  $ME(\omega)$  could very well correspond to a 43 meV peak in the ‘real’ spectrum. Finally, at  $T = 295$  K (solid line, gray solid squares) both spectra agree in showing a rather flat MMP like structure peaked around 82 meV

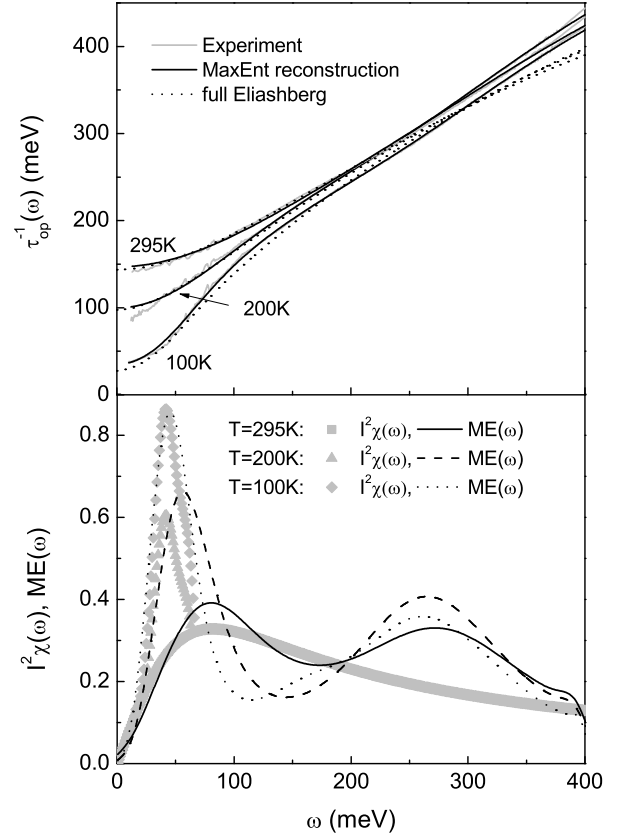


FIG. 9: Top frame: The optical scattering rate  $\tau_{op}^{-1}(\omega)$  of Bi2212 (gray solid lines) reconstructed using the MaxEnt method (solid line) for various temperatures, namely  $T = 100$  K, 200 K, and 295 K. The dotted lines correspond to data generated by full Eliashberg theory using the  $I^2\chi(\omega)$  spectra reported by Schachinger and Carbotte.<sup>35</sup> Bottom frame: The spectral function  $ME(\omega)$  (solid line for 295 K, dashed for 200 K, and dotted for 100 K) as a result of the MaxEnt inversion of the experimental data (gray solid lines in the top frame of this figure). The gray solid symbols (solid squares for 295 K, solid up-triangle for 200 K, and solid diamonds for 100 K) show the  $I^2\chi(\omega)$  spectra reported by Schachinger and Carbotte.<sup>35</sup>

with no indication of a resonance peak. This analysis corroborates the results reported by Tu *et al.*<sup>30</sup> and by Schachinger and Carbotte.<sup>35</sup>

It is quite important to notice that all  $ME(\omega)$  spectra develop a second structure of comparable height around  $\sim 260$  meV for all temperatures. Such a structure is missing in the  $I^2\chi(\omega)$  spectra. This additional structure is required for a faithful reconstruction of the data at higher energies. Thus, it seems to be a real and new feature. It proves that the charge carrier-exchange boson spectral function  $I^2\chi(\omega)$  in the cuprates will have non-zero contributions up to at least 400 meV, a property which cannot be explained by a pure phonon mechanism.

In Fig. 10 the residual  $r(\omega)$  of our analysis of the Bi2212 data is presented. The top frame is for 100 K, the

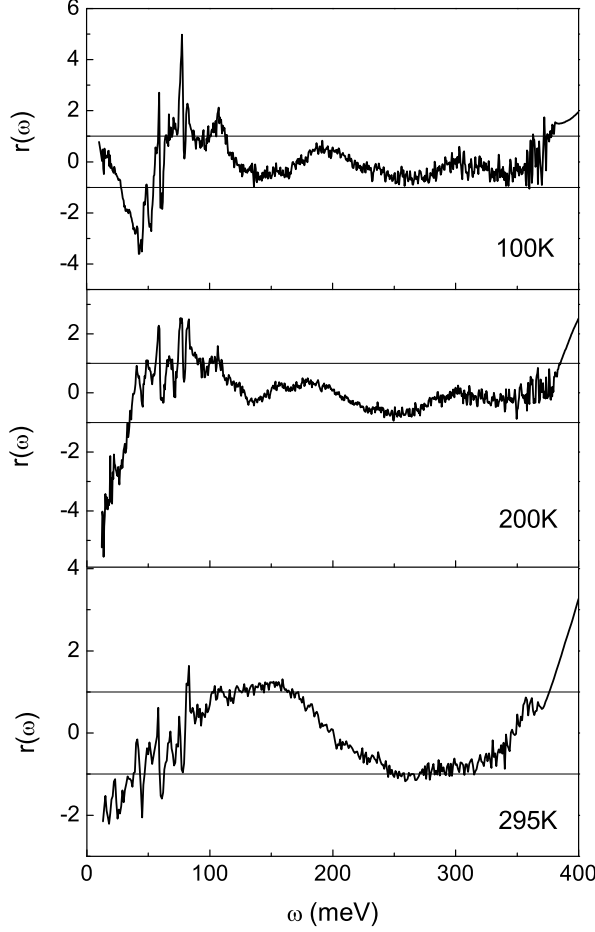


FIG. 10: The residual  $r(\omega)$  of the data reconstruction presented in the top frame of Fig. 9. The top frame is for  $T = 100$  K, the middle frame for 200 K, and the bottom frame for 295 K.

middle frame for 200 K, and the bottom frame for 295 K. The residual clearly shows a stochastic component which is much smaller than the assumed values for  $\sigma$  in the energy region  $100 \leq \omega \leq 350$  meV. It can be identified as a noise contribution. There is obviously, another slowly oscillating contribution to  $r(\omega)$  which is almost identical in frequency at 100 and 200 K but doubles its period at 295 K. This contribution is very likely to be a background signal  $B(\omega)$  generated by the experimental equipment.

We proceed to investigate superconducting state data. We use the spectral function  $I^2\chi(\omega)$  reported by CSB. It was derived from superconducting state optical scattering rates reported by Basov *et al.*<sup>46</sup> at  $T = 10$  K for an optimally doped, twinned YBCO single crystal. This  $I^2\chi(\omega)$  is based on the normal state  $I^2\chi(\omega)$  for YBCO which is an MMP form (15) with  $I^2 = 0.83$  and  $\omega_{SF} = 20$  meV. Superimposed is a pronounced peak at  $\omega = 41$  meV which was found by applying the second

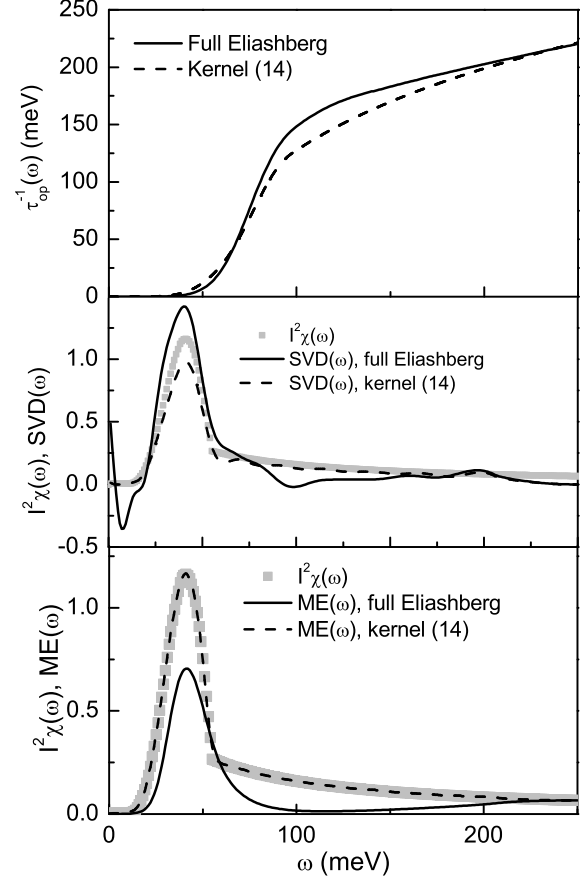


FIG. 11: Top frame: The superconducting state optical scattering rate  $\tau_{op}^{-1}(\omega)$  at  $T = 10$  K calculated from full Eliashberg theory (solid line) and using kernel (14) (dashed line) and the  $I^2\chi(\omega)$  spectrum shown as the gray solid squares in the middle and bottom frame of this figure. Middle frame: The gray solid squares correspond to the spectral function  $I^2\chi(\omega)$  reported by CSB for superconducting YBCO at  $T = 10$  K. The solid line shows the spectral function  $SVD(\omega)$  as a result of an SVD inversion of the full Eliashberg result (solid line in the top frame of this figure). The dashed line shows the same but now the scattering rate generated by kernel (14) is used as input. Bottom frame: The same as the middle frame.  $ME(\omega)$  is the result of a MaxEnt inversion.

order derivative method to the experimental data. The final form, shown using gray solid squares in the middle and bottom frame of Fig. 11, was established by a fit of full Eliashberg results to experiment.

The top frame of Fig. 11 presents the superconducting state optical scattering rate  $\tau_{op}^{-1}(\omega)$  at  $T = 10$  K as a function of energy. The solid line gives the result of a full Eliashberg calculation using the solutions of Eqs. (B1) and (B2) on the basis of the spectral function  $I^2\chi(\omega)$  just described. Eliashberg theory also provides a value for the zero temperature gap amplitude  $\Delta_0 = 22.34$  meV.

The dashed line presents the optical scattering rate as calculated using kernel (14), the above value for  $\Delta_0$ , and the same spectral function  $I^2\chi(\omega)$ . The two results differ substantially in the energy region  $70 \leq \omega \leq 200$  meV.

The results of an SVD inversion are shown in the middle frame of Fig. 11. The solid line presents the spectral function SVD( $\omega$ ) found from inverting the full Eliashberg results (solid line in the top frame of this figure) on the basis of kernel (14) using  $\Delta_0 = 22.34$  meV as an external parameter. The dashed line corresponds to the inversion of the scattering rate generated by kernel (14) using the same value for  $\Delta_0$ . In both cases the svcs threshold was set to  $10^{-2}$ . The agreement of both spectra SVD( $\omega$ ) with the original  $I^2\chi(\omega)$  is rather poor keeping in mind that the inversion is based on computer generated data.

The bottom frame of Fig. 11 is organized as the middle frame of this figure. It presents the spectra ME( $\omega$ ) as a result of a MaxEnt inversion. For the inversion of the data generated by kernel (14) an error bar of  $\sigma = 0.01$  was assumed and no noise was added to the data. The inversion was performed using historical MaxEnt with  $\gamma^2 = N_1$  as convergence criterion. The agreement with the spectrum  $I^2\chi(\omega)$  used to generate the data is perfect as is to be expected. The inversion of full Eliashberg theory generated data (solid line) is less successful. An error bar determined by  $\sigma = 0.7$  was attached to the data but no noise was added. Furthermore,  $\Delta_0$  was reduced to 21 meV in order to keep the peak in ME( $\omega$ ) at 41 meV. The peak height is now grossly underestimated and the spectrum ME( $\omega$ ) does not show the normal state background spectrum. Such a result was to be expected because of the pronounced differences particularly in this energy region between the full Eliashberg theory generated results and the data generated by kernel (14).

We proceed and try to invert directly experimental superconducting state data in order to study the applicability of a MaxEnt inversion based on kernel (14) using ‘real’ data. The top frame of Fig. 12 presents the results of a MaxEnt data reconstruction of the original data by Basov *et al.*<sup>46</sup> reported for an optimally doped, twinned YBCO single crystal at  $T = 10$  K. We attached an error bar of  $\sigma = 3.5$  to the data and used historical MaxEnt with  $\gamma^2 = N_1$  as criterion of convergence. The inversion is based on kernel (14) and resulted in the spectrum ME( $\omega$ ) presented as solid line in the bottom frame of Fig. 12. This spectrum was found using  $\Delta_0 = 21$  meV. It allowed us to place the main peak in ME( $\omega$ ) at 41 meV. It is obvious that the inverted spectrum ME( $\omega$ ) differs quite substantially from the original  $I^2\chi(\omega)$  spectrum (gray solid squares). The low energy peak ( $\omega < 5$  meV) in ME( $\omega$ ) is caused by an attempt to use MaxEnt to extrapolate to very small energies which are not supported by input data. Nevertheless, the data reconstruction (solid line in the upper frame of Fig. 12) is excellent. We added for comparison (dashed line in the upper frame of Fig. 12) the optical scattering rate as generated by full Eliashberg theory. The agreement with the data does not seem to be good enough to justify the

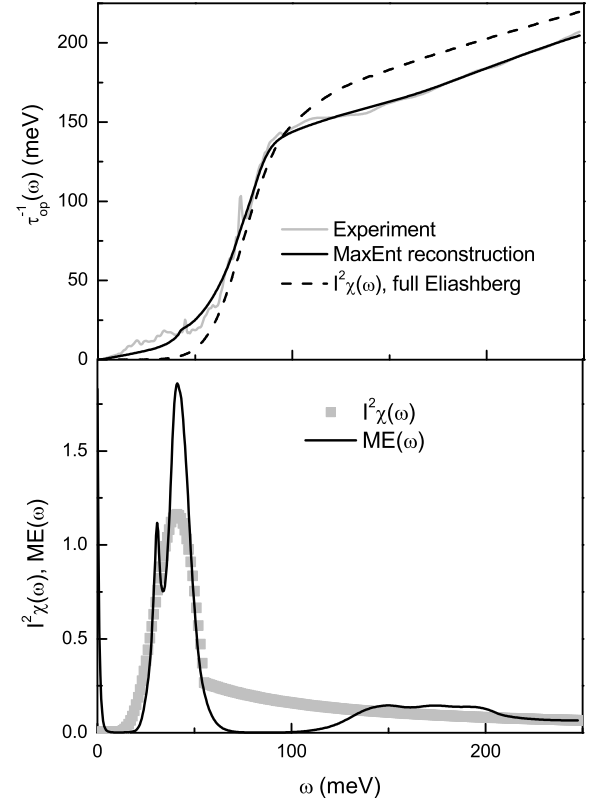


FIG. 12: Top frame: The superconducting state optical scattering rate at  $T = 10$  K for an optimally doped, twinned YBCO single crystal. The solid gray line presents the original data by Basov *et al.*<sup>46</sup>. The solid line shows the MaxEnt reconstruction of the input data while the dashed line shows the result of a full Eliashberg theory calculation based on the spectrum  $I^2\chi(\omega)$  reported by CSB for  $T = 10$  K. Bottom frame: Gray solid squares present the  $I^2\chi(\omega)$  spectrum suggested by CSB for superconducting YBCO at  $T = 10$  K. The solid line shows the spectrum ME( $\omega$ ) as a result of the inversion of the experimental data by Basov *et al.*<sup>46</sup> shown as the solid gray line in the top frame of this figure.

particular shape of  $I^2\chi(\omega)$  discussed above. Nevertheless, one has to keep in mind that all calculations presented here are performed without including impurities, i.e.: in the pure case limit. Adding impurities improves the agreement between full Eliashberg theory and experiment substantially.<sup>35</sup>

As a last example we present the reconstruction of superconducting state optical scattering rate data reported by Tu *et al.*<sup>30</sup> for an optimally doped Bi2212 single crystal at  $T = 6$  K. The results are presented in Fig. 13 which is organized the same way as Fig. 12. For the MaxEnt data reconstruction an error bar determined by  $\sigma = 3.0$  was attached to the data. Historical MaxEnt with  $\gamma^2 = N_1$  as criterion for convergence was applied. The inversion is based on kernel (14) and the spectrum  $I^2\chi(\omega)$  reported by Schachinger and Carbotte<sup>35</sup>

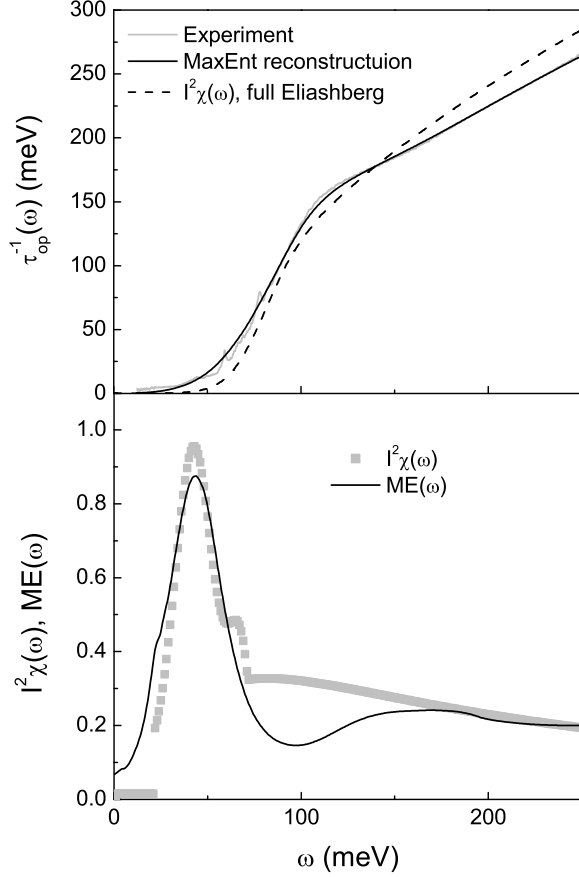


FIG. 13: The same as Fig. 12 but now for a superconducting optimally doped Bi2212 single crystal at  $T = 6$  K. The data have been reported by Tu *et al.*<sup>30</sup>

for  $T = 6$  K is shown as gray solid squares in the bottom frame of Fig. 13 for comparison. It contains a peak at 43 meV and an MMP form (15) as background with  $I^2 = 0.655$  and  $\omega_{SF} = 82$  meV. In this case the agreement between the inverted spectrum  $ME(\omega)$  (solid line in the bottom frame of Fig. 13) and  $I^2\chi(\omega)$  is much better in comparison to YBCO. This confirms the analysis of Schachinger and Carbotte<sup>35</sup> as well as a previous analysis of Bi2212 data by Schachinger and Carbotte<sup>34</sup> based on data published by Puchkov *et al.*<sup>47</sup>

### C. The least squares fit method

It has been pointed out in the previous subsection that the least squares fit method has already been applied rather successfully to invert  $I^2\chi(\omega)$  spectra from experiment using full Eliashberg theory together with additional information gathered by other means. This method is rather clumsy to handle and time consuming as one cannot develop a closed algorithm which allows one to fit parameters directly given some standard devi-

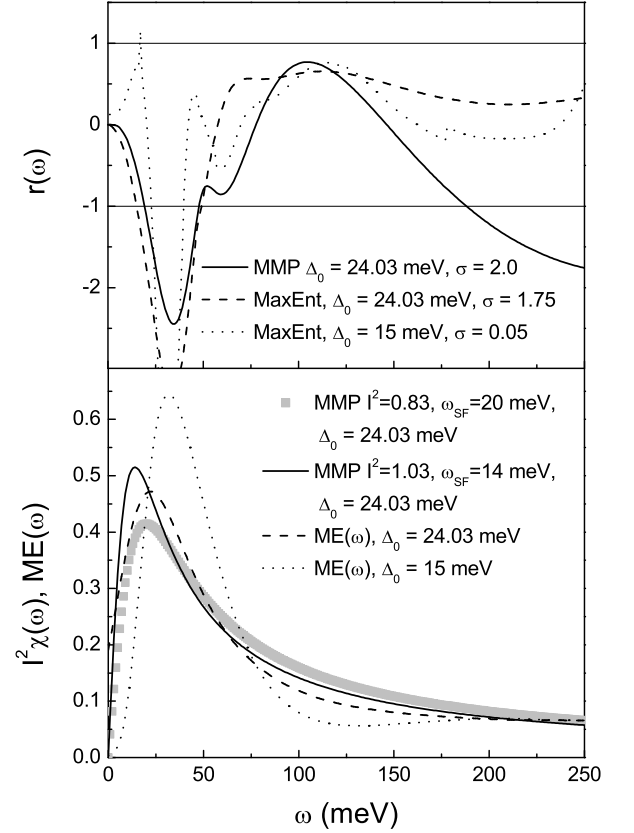


FIG. 14: Top frame: The residual  $r(\omega)$ . The solid line corresponds to a least square fit of an MMP form to computer generated optical scattering rate data generated by full Eliashberg theory,  $\Delta_0 = 24.03$  meV and  $\sigma = 2.0$  was assumed. The dashed line corresponds to a MaxEnt analysis of the same data for  $\sigma = 1.75$  keeping  $\Delta_0$  fixed and the dotted line is for  $\sigma = 0.05$  and  $\Delta_0 = 15$  meV. The main part of the various  $r(\omega)$  curves is within  $\pm 1$  indicating perfect data reconstruction within the assumed error. Bottom frame: The spectrum  $I^2\chi(\omega)$  (gray solid squares) is the input spectrum for the full Eliashberg calculation. The solid line gives the inverted spectrum as a result of a least squares fit to the data, the dashed line the result of a MaxEnt inversion both with  $\Delta_0 = 24.03$  meV. Finally, the dotted line shows the spectrum  $ME(\omega)$  which resulted from an optimal data reproduction using MaxEnt but now  $\Delta_0 = 15$  meV.

ation  $\sigma$  which plays the role of the nuisance parameter. Therefore, we want to study the least squares fit method based on an approximate kernel using experimental data  $\tau_{ex}^{-1}(\omega)$  generated by full Eliashberg theory.

In particular, we will study the least squares fit method based on the approximate kernel (14) for the zero temperature superconducting state of a  $d$ -wave superconductor. The  $\tau_{ex}^{-1}(\omega)$  data has been generated by full Eliashberg theory in the superconducting state at  $T = 10$  K using for  $I^2\chi(\omega)$  an MMP form (15) with  $I^2 = 0.83$  and  $\omega_{SF} = 20$  meV. The zero temperature gap  $\Delta_0 = 24.03$  meV. The least squares fit method is now applied to determine  $I^2$

and  $\omega_{SF}$  of an MMP form by a least squares fit to  $\tau_{ex}^{-1}(\omega)$  in the energy region  $0 \leq \omega \leq 250$  meV. The error bar attached to the input data is given by  $\sigma = 2.0$ . (This particular value of the standard deviation appears to be a realistic value for data reconstruction of ‘real’ data as was demonstrated in the previous subsection.) A consistent data reconstruction was achieved by the parameters  $I^2 = 1.03$  and  $\omega_{SF} = 14$  meV. This becomes apparent from Fig. 14 in which the results of the least squares method are illustrated. The solid line in the top frame of this figure shows the residual  $r(\omega)$ , Eq. (5), which is on average well within the assumed  $\sigma$ . This insures a correct data reconstruction. The bottom frame of this figure compares the least squares fit spectrum (solid) line to the original  $I^2\chi(\omega)$  indicated by gray solid squares. It is interesting to compare the areas under these two spectra, they are 41.5 meV and 42 meV, respectively, a difference of about 1%. The parameter  $\lambda$  which is two times the first inverse moment of  $I^2\chi(\omega)$  is also a good parameter to compare. We get  $\lambda = 3.05$  and 2.43, respectively.

Figure. 14 contains additional information. We use the MaxEnt method to generate an ‘educated guess’ for a later least squares fit to data based on full Eliashberg theory. If we use  $\Delta_0 = 24.03$  meV and assume  $\sigma = 1.75$  historical MaxEnt reproduces the input data almost equally well as our least squares fit. (Dashed line in the top frame of Fig. 14.) The resulting spectrum ME( $\omega$ ) (dashed line in the bottom frame of Fig. 14) has its peak at a slightly higher energy ( $\sim 24$  meV) as compared to the original  $I^2\chi(\omega)$  but otherwise, the input spectrum is reproduced rather well, albeit not by an MMP form. The area under this spectrum is 40 meV and  $\lambda = 3.22$ , again close to the result of the least squares fit ‘inversion’. We also include, for comparison, the result of a MaxEnt deconvolution with the emphasis on optimal data reconstruction. We reduce the error bar on the input data to  $\sigma = 0.05$  and use  $\Delta_0$  as a parameter to be adjusted in order to achieve this goal. An almost perfect reproduction is possible if  $\Delta_0$  is reduced to 15 meV. This becomes apparent from the residual  $r(\omega)$  shown as a dotted line in the top frame of Fig. 14. The resulting spectrum ME( $\omega$ ) is presented by a dotted line in the bottom frame of Fig. 14. The peak is now shifted to much higher energies, it is wider, and is of greater height compared to the original  $I^2\chi(\omega)$ . The area under the spectrum is 40.2 meV and  $\lambda = 1.92$ .

As a result of this study one can say that given additional information, like the value of the zero temperature gap, both methods, least square fit and MaxEnt, result in comparable spectra, nevertheless, they differ qualitatively and quantitatively from the ‘real’ spectrum  $I^2\chi(\omega)$ . This emphasizes the role of additional information beyond the optical data for a successful data analysis.

## IV. CONCLUSION

There exists a well established formalism that relates the electron-phonon spectral density  $\alpha^2F(\omega)$  to the infrared conductivity. It applies to the superconducting as well as normal state and involves the Eliashberg equations plus a Kubo formula which gives  $\sigma_{op}(\omega)$  from Green’s functions. While such a formalism is not as well justified in the case of other boson exchange mechanisms such as spin fluctuations, it has, nevertheless, been useful to apply it as a first approximation with appropriate modifications such as to  $d$ -wave gap symmetry. The equations involved are, however, rather complicated and approximate, simplified expressions for the relationship between spectral density  $I^2\chi(\omega)$  and optical conductivity have played an important role particularly if a main aim is to extract qualitative rather than quantitative information on the size and main features of the  $I^2\chi(\omega)$  for a given set of optical data. If, however, accurate quantitative information is desired a full Eliashberg formulation cannot be avoided. In this paper we provided comparison between numerical results for the optical scattering rate  $\tau_{op}^{-1}(\omega)$  based on the exact equations and results generated from several often used approximate relations between conductivity and spectral density including a recent generalization which applies to a superconductor at  $T = 0$  with  $d$ -wave symmetry.

Another important issue discussed in detail is the accuracy, advantages, and limitations of various numerical methods which are needed to invert data even within the limitations of approximate formulas for the optical scattering rate. These equations relate the optical scattering rate measured in infrared experiments to the desired spectral density  $I^2\chi(\omega)$  through an integration involving a known, specified kernel  $K(\Omega, \omega; T)$  multiplied by  $I^2\chi(\omega)$ . Deconvoluting (inverting) such an integral is an ill defined mathematical problem. Nevertheless, various inversion techniques can be applied. Here we have tested three, namely singular value decomposition, maximum entropy, and least squares fit of a few parameters which characterize the assumed mathematical form of  $I^2\chi(\omega)$ . We conclude that for the problem at hand maximum entropy or least squares fitting are the methods to be preferred. All have their limitations, however, and in some cases it will also be necessary to go back to the full Kubo formula and Eliashberg equations. In the latter case a least squares fit based on approximate results from MaxEnt appears to be the most successful strategy.

## Acknowledgment

Research supported in part by the Natural Sciences and Engineering Research Council of Canada (NSERC), by the Canadian Institute for Advanced Research (CIAR), and by Fonds zur Förderung der Wissenschaftlichen Forschung (Vienna) under contract No. P15834-PHY. We thank D.N. Basov for interest and dis-

cussion. Two of us (D.N. and E.S.) are indebted to W. von der Linden for discussions, support, and his interest in this work.

## APPENDIX A: THE MAXIMUM ENTROPY METHOD FOR DATA ANALYSIS

The direct inversion of Eq. (8) constitutes an ill-posed problem. Therefore, there are many different ‘solutions’ (varying orders of magnitude) that fit the data within the error bars. The most general solution to this problem is the calculation of the *posterior* probability distribution (pdf)  $p(\mathbf{a}|\mathbf{t}, \mathcal{I})$  of possible solutions  $\mathbf{a}$  given the data  $\mathbf{t}$  and all additionally available background information  $\mathcal{I}$ , i.e.: the matrix  $\mathbf{K}$  which is defined by the underlying theoretical model, the background function  $B(\omega)$ , the noise contribution  $\eta(\omega)$ , etc. Bayesian probability theory<sup>41</sup> provides the consistent framework for such a fully probabilistic description. Bayes’ theorem provides the relation

$$p(\mathbf{a}|\mathbf{t}, \mathcal{I}) = \frac{p(\mathbf{t}|\mathbf{a}, \mathcal{I})p(\mathbf{a}|\mathcal{I})}{p(\mathbf{t}|\mathcal{I})}, \quad (\text{A1})$$

which relates the posterior  $p(\mathbf{a}|\mathbf{t}, \mathcal{I})$  to the *likelihood* pdf  $p(\mathbf{t}|\mathbf{a}, \mathcal{I})$  and the *prior* pdf  $p(\mathbf{a}|\mathcal{I})$ . Finally, the denominator  $p(\mathbf{t}|\mathcal{I})$  ensures proper normalization of the posterior. The likelihood comprises the model definition and the error statistics of the data. Its knowledge is an essential prerequisite for any data analysis. The prior, on the other hand, should incorporate all available information of the problem at hand. In the particular case discussed here, the only known constraint is the positivity of the function values  $a_j \equiv \alpha^2 F(\Omega_j)$ .

Skilling<sup>48</sup> showed that the most uninformative prior in this case is the Maximum Entropy prior:

$$p(\mathbf{a}|\alpha, \mathcal{I}) = \exp(\alpha S) \left( \prod_{j=1}^{N_2} \sqrt{a_j} \right)^{-1}. \quad (\text{A2})$$

Here,  $\alpha$  is a renormalization (nuisance) parameter and  $S$  is the generalized Shannon-Jaynes entropy<sup>41</sup>

$$S = \sum_{j=1}^{N_2} \left[ a_j - m_j - a_j \log \frac{a_j}{m_j} \right]. \quad (\text{A3})$$

It measures the distance of the candidate vector  $\mathbf{a}$  from the so-called *default model* vector  $\mathbf{m} = \{m_j | j = 1, \dots, N_2\}$ , which represents the most probable solution prior the observation of any data. In case of insufficient background information it should be chosen constant, i.e.:  $m_j \equiv \text{const}, \forall j$ . Nevertheless, it is adamant to check its influence on the solution, as certain features of the solution might not be supported by the data but instead just reflect the initial assumption of the default model.

The regularization parameter  $\alpha$  determines the relative influence of the prior compared to the likelihood. In

the limit  $\alpha \rightarrow \infty$  one obtains  $\mathbf{a} \rightarrow \mathbf{m}$  as the most probable solution; for  $\alpha \rightarrow 0$ , on the other hand, one gets the maximum likelihood solution which will be meaningless for ill-conditioned problems. Within conventional approaches, regularization parameters such as  $\alpha$  are often fixed by hand. Apart from ad-hoc settings, a sensible choice is to adjust the regularization parameter such that the expectation value of the misfit  $\gamma^2$  is reproduced.<sup>49</sup> In case of an  $N$ -dimensional uncorrelated normal distribution the misfit is described by the  $\chi^2$ -distribution with  $N$  degrees of freedom and has mean  $\langle \gamma^2 \rangle = N$  and variance  $\text{var}(\gamma^2) = 2N$ . Historically, the criterion  $\gamma^2 = N$  was employed first in order to fix the parameter  $\alpha$  (historical MaxEnt). However, one has to keep in mind that the solution might change dramatically if the regularization parameter  $\alpha$  is tuned such that  $\gamma^2$  varies between  $N - \sqrt{2N} \leq \gamma^2 \leq N + \sqrt{2N}$ .

In principle, the regularization parameter  $\alpha$  can be determined consistently within Bayesian probability theory by computing the most probable value  $\alpha$  which maximizes the probability  $p(\alpha|\mathbf{t}, \mathcal{I})$  given the data  $\mathbf{t}$ . (This is the classical MaxEnt of Ref. 50.) Unfortunately, the calculation of  $p(\alpha|\mathbf{t}, \mathcal{I})$  involves high dimensional integrals which can only be evaluated using rather crude simplifications. The approximation usually applied<sup>50</sup> tends to overfit the data as  $p(\alpha|\mathbf{t}, \mathcal{I})$  is systematically overestimated for small  $\alpha$  which results in a too small  $\hat{\alpha}$ -value at which  $p(\alpha|\mathbf{t}, \mathcal{I})$  has its maximum as a function of  $\alpha$ . Von der Linden<sup>51</sup> suggested a different approximation scheme that partly corrects these deficiencies and yields results similar to the historic criterion.

For some data sets analyzed in the study, we found that all methods to determine the value of  $\alpha$  suffered from oscillations (‘ringing’) due to overfitting. This has been observed for other applications as well.<sup>52,53</sup> To a certain extent, this ringing is intrinsic to the MaxEnt prior which explicitly treats all points of the reconstruction  $\mathbf{a}$  as uncorrelated.

In order to enforce smoothness of the solution Skilling<sup>54</sup> suggested the introduction of a ‘hidden image’  $\mathbf{h}$  which is blurred by a Gaussian

$$a_j = \sum_k B_{jk} h_k, \quad B_{jk} = \frac{1}{\sqrt{2\pi}b^2} \exp \left[ -\frac{(x_j - x_k)^2}{2b^2} \right]. \quad (\text{A4})$$

Here, the  $x_j$  designate the abscissas of  $a_j$  and  $h_j$ . The vector  $\mathbf{a}$  enters the likelihood, while  $\mathbf{h}$  is used to compute the entropy  $S$ . The blur-width  $b$  is an additional hyperparameter that can be determined simultaneously with  $\alpha$  by locating the maximum of  $p(b, \alpha|\mathbf{t}, \mathcal{I})$  given the data  $\mathbf{t}$  in the spirit of Ref. 54.

Various choices of the blur-width  $b$  can be regarded as distinct models which have a different number of degrees of freedom (similar to fit functions involving different numbers of parameters). For  $b \rightarrow 0$  all positive discrete representations  $\mathbf{a}$  can be realized as  $\mathbf{a} \rightarrow \mathbf{h}$ , while in the limit  $b \rightarrow \infty$  only constant functions  $a_i \equiv \text{const.}$  can be represented, i.e.: the model has only one effective



degree of freedom.

The optimal blur-width  $b$  is determined by the interplay of the likelihood and Occam's razor<sup>41,53</sup> which penalizes the complexity of the model employed and is implicit in the calculation of  $p(b, \alpha | \mathbf{t}, \mathcal{I})$ . The 'penalty factor' is the ratio of the width of the likelihood and the prior distributions. Thus, a simpler model may be more favorable because a larger fraction of the parameter space is likely to be realized according to data although a more complex model fits the data better.

Unless stated otherwise, we have determined the optimal blur-width  $b$  for the MaxEnt reconstructions presented in Sec. III as outlined above. For the computation of  $p(b | \mathbf{t}, \mathcal{I})$  we chose a flat prior  $p(b | \mathcal{I})$  on the interval  $b_{min} \leq b \leq b_{max}$  with  $b_{min} \sim x_2 - x_1$  and  $b_{max} \sim x_N - x_1$ .

The MaxEnt method obviously allows for an explicit treatment of ambiguous solutions and it allows prior knowledge to be taken into account consistently by introducing a suitable prior pdf. A direct inversion, like the SVD method, which may be badly conditioned or may involve uncontrolled approximations, is avoided. Finally, it is possible to obtain error estimates. Nevertheless, it has to be pointed out that 'fuzzy' constraints such as smoothness of the output of the inversion process make a definition of the prior pdf rather complicated.<sup>55</sup>

## APPENDIX B: ELIASHBERG EQUATIONS

The generalized Eliashberg Equations which play an important role in this study are

$$\begin{aligned} \tilde{\Delta}(\nu + i0^+; \theta) = & \pi T g \sum_{m=0}^{\infty} \cos(2\theta) [\lambda(\nu - i\omega_m) + \lambda(\nu + i\omega_m)] h(i\omega_m) \\ & + i\pi g \int_{-\infty}^{\infty} dz \cos(2\theta) I^2 \chi(z) [n(z) + f(z - \nu)] h(i\omega_m \rightarrow \nu - z + i0^+), \end{aligned} \quad (\text{B1a})$$

and, in the renormalization channel,

$$\begin{aligned} \tilde{\omega}(\nu + i0^+) = & \nu + i\pi T \sum_{m=0}^{\infty} [\lambda(\nu - i\omega_m) - \lambda(\nu + i\omega_m)] g(i\omega_m) \\ & + i\pi \int_{-\infty}^{\infty} dz I^2 \chi(z) [n(z) + f(z - \nu)] g(i\omega_m \rightarrow \nu - z + i0^+). \end{aligned} \quad (\text{B1b})$$

Here

$$h(i\omega_m) = \left\langle \frac{\tilde{\Delta}(i\omega_m; \theta) \cos(2\theta)}{\sqrt{\tilde{\omega}^2(i\omega_m) + \tilde{\Delta}^2(i\omega_m; \theta)}} \right\rangle_{\theta}, \quad g(i\omega_m) = \left\langle \frac{\tilde{\omega}(i\omega_m)}{\sqrt{\tilde{\omega}^2(i\omega_m) + \tilde{\Delta}^2(i\omega_m; \theta)}} \right\rangle_{\theta},$$

and the parameter  $g$  allows for a possible difference in spectral density between  $\tilde{\omega}$  and  $\tilde{\Delta}$  channels. It is fixed to get the measured value of the critical temperature. In the above  $\tilde{\Delta}(i\omega_m; \theta)$  is the pairing energy evaluated at the fermionic Matsubara frequencies  $\omega_m = \pi T(2m - 1)$ ,  $m = 0, \pm 1, \pm 2, \dots$ ;  $f(z)$  and  $n(z)$  are the Fermi and Bose distribution, respectively. The renormalized Matsubara frequencies are  $\tilde{\omega}(i\omega_m)$ . The analytic continuation to real frequencies  $\nu$  of the above is  $\tilde{\Delta}(\nu + i0^+; \theta)$  and  $\tilde{\omega}(\nu + i0^+)$ . The brackets  $\langle \dots \rangle_{\theta}$  are the angular average over  $\theta$ , and  $\lambda(\nu) = \int_{-\infty}^{\infty} d\Omega I^2 \chi(\Omega) / (\nu - \Omega + i0^+)$ . Eqs. (B1) are a set of nonlinear coupled equations for the renormalized pairing potential  $\tilde{\Delta}(\nu + i0^+; \theta)$  and the normalized frequencies  $\tilde{\omega}(\nu + i0^+)$  with the gap  $\Delta(\nu + i0^+; \theta) = \tilde{\Delta}(\nu + i0^+; \theta) / Z(\nu)$ , where the renormalization function  $Z(\nu)$  was introduced in the usual way as  $\tilde{\omega}(\nu + i0^+) = \nu Z(\nu)$ . To get the  $s$ -wave version of these equations  $g$  is set equal to one and all  $\cos(2\theta)$  factors are to be omitted with no average over the polar angle  $\theta$ . A Coulomb pseudopotential  $\mu^*$  must also be introduced in Eq. (B1a).

The optical conductivity follows from knowledge of  $\tilde{\omega}$  and  $\tilde{\Delta}$ . The formula to be evaluated is

$$\sigma_{op}(T, \nu) = \frac{\Omega_p^2}{4\pi} \frac{i}{\nu} \left\langle \int_0^{\infty} d\omega \tanh\left(\frac{\beta\omega}{2}\right) [J(\omega, \nu) - J(-\omega, \nu)] \right\rangle_{\theta}. \quad (\text{B2})$$

The function  $J(\omega, \nu)$  is given by

$$2J(\omega, \nu) = \frac{1 - N(\omega; \theta)N(\omega + \nu; \theta) - P(\omega; \theta)P(\omega + \nu; \theta)}{E(\omega; \theta) + E(\omega + \nu; \theta)} + \frac{1 + N^*(\omega; \theta)N(\omega + \nu; \theta) + P^*(\omega; \theta)P(\omega + \nu; \theta)}{E^*(\omega; \theta) - E(\omega + \nu; \theta)}, \quad (\text{B3})$$

with  $E(\omega; \theta) = \sqrt{\tilde{\omega}^2(\omega + i0^+) - \tilde{\Delta}^2(\omega + i0^+; \theta)}$ ,  $N(\omega; \theta) = \tilde{\omega}(\omega + i0^+)/E(\omega; \theta)$ , and  $P(\omega; \theta) = \tilde{\Delta}(\omega + i0^+; \theta)/E(\omega; \theta)$ . Finally, the star refers to the complex conjugate.

- 
- \* Electronic address: schachinger@itp.tu-graz.ac.at; URL: [www.itp.tu-graz.ac.at/~ewald](http://www.itp.tu-graz.ac.at/~ewald)
- <sup>1</sup> F. Marsiglio and J.P. Carbotte, in *The Physics of Superconductivity: Conventional and High-Tc Superconductors*, edited by K.-H. Bennemann and J.B. Ketterson (Springer, Berlin, 2003) Vol. I, p. 233.
  - <sup>2</sup> J.P. Carbotte, Rev. Mod. Phys. **62**, 1027 (1990).
  - <sup>3</sup> P.B. Allen, Phys. Rev. B **3**, 305 (1971).
  - <sup>4</sup> J.P. Carbotte, E. Schachinger, and J. Hwang, Phys. Rev. B **71**, 054506 (2005).
  - <sup>5</sup> W.L. McMillan and J.M. Rowell, Phys. Rev. Lett. **14**, 68 (1965).
  - <sup>6</sup> B. Farnworth and T. Timusk, Phys. Rev. B **10**, 2799 (1974); Phys. Rev. B **14**, 5119 (1976).
  - <sup>7</sup> P. Tomlinson and J.P. Carbotte, Phys. Rev. B **13**, 4738 (1976).
  - <sup>8</sup> B. Mitrović and M.A. Fiorucci, Phys. Rev. B **31**, 2694 (1985).
  - <sup>9</sup> B. Mitrović and S. Perkowitz, Phys. Rev. B **30**, 6749 (1984).
  - <sup>10</sup> F. Marsiglio, T. Startseva, and J. P. Carbotte, Physics Lett. A **245**, 172 (1998).
  - <sup>11</sup> A. V. Chubukov, D. Pines, and J. Schmalian, in: *The Physics of Superconductivity: Conventional and High-Tc Superconductors*, edited by K.-H. Bennemann and J. B. Ketterson (Springer, Berlin, 2003), Vol. I, p. 495.
  - <sup>12</sup> P. Monthoux and D. Pines, Phys. Rev. B **47**, 6069 (1993); Phys. Rev. B **49**, 4261 (1994).
  - <sup>13</sup> M.L. Kulić, Phys. Rep. **338**, 1 (2000).
  - <sup>14</sup> R. Zeyher and M.L. Kulić, Phys. Rev. B **53**, 2850 (1996); **54**, 8985 (1996).
  - <sup>15</sup> M.L. Kulić and R. Zeyher, Phys. Rev. B **49**, R4395 (1994); Physica C **199-200**, 358 (1994); **235-240**, 358 (1994).
  - <sup>16</sup> M. Weger, B. Barbelini, and M. Peter, Z. Phys. B **94**, 387 (1994).
  - <sup>17</sup> M. Weger, M. Peter, and L.P. Pitaevskii, Z. Phys. B **101**, 573 (1996).
  - <sup>18</sup> O.V. Danylenko, O.V. Dolgov, M.L. Kulić, and V. Oudovenko, Euro. Phys. Jour. B-Cond. Matter **9**, 201 (1999).
  - <sup>19</sup> M.L. Kulić and O.V. Dolgov, in *High Temperature Superconductivity*, edited by S. Barnes, J. Ashkenazi, J. Cohn, and F. Zuo, AIP Conf. Proc. No. 483 (AIP, Woodbury, NY, 1999), p. 63.
  - <sup>20</sup> E. Schachinger and J.P. Carbotte, in: *Models and Methods of High-TC Superconductivity: some Frontal Aspects*, edited by J.K. Srivastava and S.M. Rao, (Nova Science, Hauppauge, NY, 2003), Vol. II, pp. 73.
  - <sup>21</sup> J.F. Zasadzinski, L. Ozyuzer, N. Miyakawa, K.E. Gray, D.G. Hinks, and C. Kendziora, Phys. Rev. Lett. **87**, 067005 (2001).
  - <sup>22</sup> J.F. Zasadzinski, L. Coffey, P. Romano, and Z. Yusof, Phys. Rev. B **68**, 180504(R) (2003).
  - <sup>23</sup> J.F. Zasadzinski, L. Ozyuzer, L. Coffey, K.E. Gray, D.G. Hinks, and C. Kendziora, cond-mat/0510057 (unpublished).
  - <sup>24</sup> A. Kaminski, M. Randeria, J.C. Campuzano, M.R. Norman, H. Fretwell, J. Mesot, T. Sato, T. Takahashi, and K. Kadowaki, Phys. Rev. Lett. **86**, 1070 (2001).
  - <sup>25</sup> J.C. Campuzano, H. Ding, M.R. Norman, H.M. Fretwell, M. Randeria, A. Kaminski, J. Mesot, T. Takeuchi, T. Sato, T. Yokoya, T. Takahashi, T. Mochiku, K. Kadowaki, P. Guptasarma, D.G. Hinks, Z. Konstantinovic, Z.Z. Li, and H. Raffy, Phys. Rev. Lett. **83**, 3709 (1999).
  - <sup>26</sup> M.R. Norman, M. Eschrig, A. Kaminski, and J.C. Campuzano, Phys. Rev. B **64**, 184508 (2001).
  - <sup>27</sup> M. Eschrig and M.R. Norman, Phys. Rev. Lett. **85**, 3261 (2000).
  - <sup>28</sup> T. Cuk, F. Baumberger, D.H. Lu, N. Ingle, X.J. Zhou, H. Eisaki, N. Kaneko, Z. Hussain, T.P. Devereaux, N. Nagaosa, and Z.X. Shen, Phys. Rev. Lett. **93**, 117003 (2004).
  - <sup>29</sup> J. P. Carbotte, E. Schachinger, and D. Basov, Nature (London) **401**, 354 (1999).
  - <sup>30</sup> J.J. Tu, C.C. Homes, G.D. Gu, D.N. Basov, and M. Strongin, Phys. Rev. B **66**, 144514 (2002).
  - <sup>31</sup> E. Schachinger, J.J. Tu, and J.P. Carbotte, Phys. Rev. B **67**, 214508 (2003); Physica C **364-365**, 13 (2001).
  - <sup>32</sup> J. Hwang, T. Timusk, and G.D. Gu, Nature (London) **427**, 714 (2004).
  - <sup>33</sup> A. J. Millis, H. Monien, and D. Pines, Phys. Rev. B **42**, 167 (1990).
  - <sup>34</sup> E. Schachinger and J.P. Carbotte, Phys. Rev. B **62**, 9054 (2000).
  - <sup>35</sup> E. Schachinger and J.P. Carbotte, J. Phys. Stud. **7**, 209 (2003).
  - <sup>36</sup> S.V. Dordevic, C.C. Homes, J.J. Tu, T. Valla, M. Strongin, P.D. Johnson, G.D. Gu, and D.N. Basov, Phys. Rev. B **71**, 104529 (2005).
  - <sup>37</sup> S.V. Shulga, O.V. Dolgov, and E.G. Maksimov, Physica C **178**, 266 (1991).
  - <sup>38</sup> S.G. Sharapov and J.P. Carbotte, Phys. Rev. B **72**, 134506 (2005).
  - <sup>39</sup> J.P. Carbotte and E. Schachinger, Ann. Phys. (in print).

- <sup>40</sup> J. Hwang, J. Yang, T. Timusk, S.G. Sharapov, J.P. Carbotte, D.A. Bonn, R. Liang, and W.N. Hardy, cond-mat/0505302 (unpublished).
- <sup>41</sup> See for instance: D.S. Sivia, *Data Analysis*, Clarendon Press, Oxford (1996).
- <sup>42</sup> J. C. Nash, *Compact Numerical Methods for Computers: Linear Algebra and Function Minimalization*, Adam Hilger, Bristol (1990), p. 30.
- <sup>43</sup> E.T. Jaynes, Phys. Rev. **106**, 620 (1957); **108**, 171 (1957).
- <sup>44</sup> R.R. Joyce and P.L. Richards, Phys. Rev. Lett. **24**, 1007 (1970).
- <sup>45</sup> D. Branch and J. P. Carbotte, Can. J. Phys. **77**, 531 (1999); Jour. Supercond. **12**, 667 (1999).
- <sup>46</sup> D.N. Basov, A.V. Puchkov, R.A. Hughes, T. Strach, J. Preston, T. Timusk, D.A. Bonn, R. Liang, and W.N. Hardy, Phys. Rev. B **49**, 12165 (1994).
- <sup>47</sup> A. Puchkov, D.N. Basov, and T. Timusk, J. Phys.: Condens. Matter **8**, 10 049 (1996).
- <sup>48</sup> J. Skilling, in: *Maximum Entropy and Bayesian Methods*, edited by J. Skilling (Kluwer, Dordrecht, 1989), pp. 45.
- <sup>49</sup> We would like to point out that in the MaxEnt literature the symbol  $\chi^2$  is used instead of  $\gamma^2$ .
- <sup>50</sup> S.F. Gull, in: *Maximum Entropy and Bayesian Methods*, edited by J. Skilling (Kluwer, Dordrecht, 1989), pp. 53.
- <sup>51</sup> W. von der Linden, R. Preuss, and V. Dose, in: *Maximum Entropy and Bayesian Methods*, edited by W. von der Linden, V. Dose, R. Fischer, and R. Preuss (Kluwer, Dordrecht, 1989), pp. 285.ei wesentliche Punkte:
- <sup>52</sup> R. Fischer, Anal. Bioanal. Chem. **374**, 619 (2002).
- <sup>53</sup> R. Fischer, W. von der Linden, and V. Dose, in: *MAX-ENT'96 - Proceedings of the Maximum Entropy Conference 1996*, edited by M. Sears, V. Nedeljkovic, N.E. Pendock, and S. Sibisi, (NMB Printers, Port Elisabeth, 1996), p. 21 and references therein.
- <sup>54</sup> J. Skilling, in: *Maximum Entropy in Action*, edited by B. Buck and V.A. Macaulay (Calrendon Press, London, 1991), p.19.
- <sup>55</sup> V. Drose, Rep. Prog. Phys. **66**, 1421 (2003).